EFFECT OF HOLD TIMES ON FATIGUE BEHAVIOR OF NEXTEL™ 720/ALUMINA CERAMIC MATRIX COMPOSITE AT 1200°C IN AIR AND IN STEAM ENVIRONMENT

THESIS

John M. Mehrman, Captain, USAF

AFIT/GAE/ENY/06-M23

DEPARTMENT OF THE AIR FORCE
AIR UNIVERSITY

AIR FORCE INSTITUTE OF TECHNOLOGY

Wright-Patterson Air Force Base, Ohio

AFIT/GAE/ENY/06-M23

EFFECT OF HOLD TIMES ON FATIGUE BEHAVIOR OF NEXTEL™ 720/ALUMINA CERAMIC MATRIX COMPOSITE AT 1200°C IN AIR AND IN STEAM ENVIRONMENT

THESIS

Presented to the Faculty

Department of Aeronautics and Astronautics

Graduate School of Engineering and Management

Air Force Institute of Technology

Air University

Air Education and Training Command

In Partial Fulfillment of the Requirements for the

Degree of Master of Science in Aeronautical Engineering

John M. Mehrman, BS

Captain, USAF

March 2006

AFIT/GAE/ENY/06-M23

EFFECT OF HOLD TIMES ON FATIGUE BEHAVIOR OF NEXTEL™ 720/ALUMINA CERAMIC MATRIX COMPOSITE AT 1200°C IN AIR AND IN STEAM ENVIRONMENT

John M. Mehrman, BS
Captain, USAF

Approved:

// Signed //

_____   _____
Dr. Marina Ruggles-Wrenn (Chair)   date

// Signed //

_____   _____
Dr. Theodore Nicholas (Member)   date

// Signed //

_____   _____
Dr. Som Soni (Member)   date

Abstract

The aerospace field requires structural materials that can maintain superior mechanical properties while subjected to high temperatures and oxidizing environments. This research investigated the effect of hold times at maximum load on fatigue performance of a Nextel™720/Alumina ceramic matrix composite at 1200°C, explored the influence of environment on material response to cyclic loading with hold times at maximum load, and assessed the effects of loading history on material behavior and environmental durability. The N720/A composite relies on an oxide/oxide composition for inherent oxidation resistance and a porous matrix with no interphase between the fiber and matrix for damage tolerance.

Mechanical testing results showed a significant decrease in material life and performance in a steam environment when compared to tests conducted in a laboratory air environment. Prior fatigue of specimens tested in an air environment resulted in an order of magnitude increase in creep life. Fracture surface observations with a Scanning Electron Microscope showed a correlation between an increase in fiber pull-out and increased time to failure. A qualitative spectral analysis indicated evidence of silicon species migration from the mullite phase of the fiber to the matrix, especially in the steam environment. This may be the cause of the decreased creep performance of the material in the steam environment.

AFIT/GAE/ENY/06-M23

Acknowledgments

Table of Contents

List of Figures

List of Tables

EFFECT OF HOLD TIMES ON FATIGUE BEHAVIOR OF NEXTEL™

720/ALUMINA CERAMIC MATRIX COMPOSITE AT 1200°C IN AIR AND IN

STEAM ENVIRONMENT

I. Introduction

Advances in materials and our understanding of their properties have provided the basis for much of our technological development over the years. The inventions of gun powder and steel gave rise to monumental changes in the ways we live, and the fabric of our societies. In our ever increasing push for technological advancement, it is often materials that bound our progress. By understanding these bounds and improving upon them, we can continue to strive forward.

While composite materials have been used for thousands of years, since times when straw and clay were combined to make a stronger brick, recent developments in and needs of the aerospace industries have called for more advanced composite materials. Composite materials made their appearance in commercial airplanes with the introduction of the Boeing 707 in the 1950s. Today, composites make up a large percentage of aircraft structural components. Composites comprise 9% of the aircraft structural weight in the Boeing 777. Boeing is predicting that 50% of the material used on the 787 Dreamliner, scheduled for delivery in 2010, will be composites [5].

The US Air Force, and the aerospace industry as a whole, has a strong interest in the continued development of composites. Advances in propulsion technologies have raised the demand for materials that have to perform at high loads while at high

temperatures. The US Air Force Integrated High Performance Turbine Engine

Technology (IHPTET) program was established in 1987 with a goal to double aircraft

propulsion capability [14]. This led to an increased interest Ceramic Matrix Composites

(CMCs), which exhibit and maintain high strength at elevated temperatures. Many

potential applications for CMC's arose including combustor liners and turbine vanes.

      However, CMCs were found to be susceptible to oxidation in the turbine engine

operating environment. Oxide/Oxide CMCs were developed to combat the

environmental degradation. These materials use oxide based ceramics such as alumina

(Al_2O_3) that have an inherent resistance to oxidation. While oxidation effects were

reduced, creep resistance and other aspects of the material performance were below the

required levels. Research continues on how to provide structural materials that

demonstrate the strength, temperature, and oxidation resistance needed by the aerospace

industry.

      Recent efforts [10;11;29] investigated the mechanical behavior of the

N720/alumina composite at 1200°C in laboratory air and steam environments. Harlan

[11;29] reported on the effect of environment on creep resistance, while Eber [10;29]

focused on fatigue durability. The purpose of the present research is to investigate the

effect of hold times at maximum load on fatigue performance of N720/A at 1200°C,

explore the influence of environment on material response to cyclic loading with hold

times at maximum load, and, finally, to assess the effects of loading history on material

behavior and environmental durability. Furthermore, this effort aims to understand and

elucidate the microstructural damage and failure mechanisms, so that improvements in

the CMC design and processing can be attempted.

II. Background

2.1 Ceramic Matrix Composites

The term "ceramic" can be applied to a wide range of materials. Ceramics are typically inorganic and non-metallic in nature, consisting of a combination of metallic and non-metallic elements with a crystalline structure [3]. Ceramics generally exhibit high strength, hardness, and heat resistance. It is their high temperature strength that makes these materials particularly attractive to the aerospace design community. Figure 1 shows the maximum service temperature of polymers, metals and ceramics [7:5]. Ceramics are the only class of material that can reliably be used at temperatures above 1100°C.
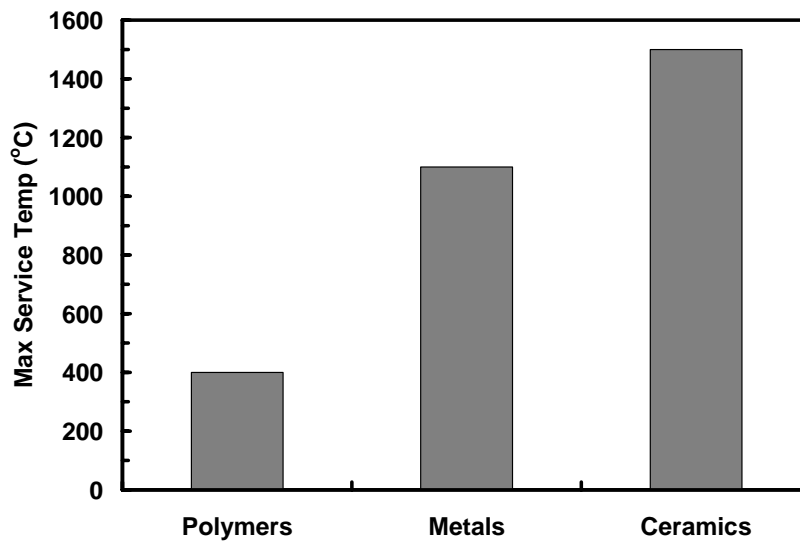
Figure 1. Maximum service temperature of polymers, metals and ceramics [7:5].

On the negative side, ceramics tend to be brittle, with low fracture toughness and damage tolerance. While metals can deform plastically before fracture, a process that involves extensive energy dissipation, monolithic ceramics do not show signs of plastic deformation and fail in a catastrophic fashion [7:4]. It is this catastrophic failure that makes application of monolithic ceramics difficult in load bearing structures.

A composite is "… a material system consisting of two or more phases on a macroscopic scale, whose mechanical performance and properties are designed to be superior to those of the constituent materials acting independently" [9:3]. Typically there are two phases to the material system, a discontinuous reinforcement phase and a continuous matrix phase. Figure 2 shows the phases of a typical composite. The reinforcement can be in the form of fibers, whiskers, or particles. By combining two or more materials, the mechanical properties can be specifically tailored to the needed application, with the number of permutations of material combinations being enormous.
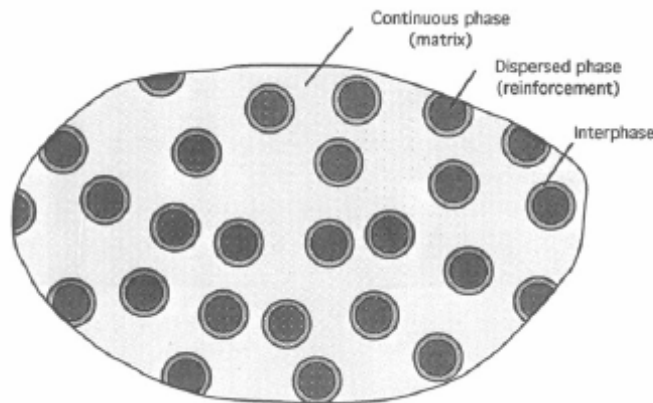
Figure 2. Phases of typical composite [9:1].

Ceramic matrix composites are designed to combine the high temperature resistance of ceramics with higher fracture toughness. Energy dissipating phenomena such as fiber matrix debonding, crack deflection, fiber bridging and fiber pullout inherent in CMCs, significantly raise the damage tolerance of the material [7:8]. This permits the use of CMCs in applications where monolithic ceramics can not be employed.

The matrix of the composite has three main functions. The matrix transfers load between fibers, separates the fibers to prevent adjacent fibers from failing after the first fiber failure, and protects the fibers from environmental effects [4:7]. While the matrix material alone may not have particularly good toughness characteristics, it is the matrix phase that serves to improve the toughness of the overall composite. The matrix provides for the flaw tolerance of the CMC by relieving stress concentrations on the fiber. Different methods of accomplishing this are discussed further in section 2.2 below.

Ceramic fibers exhibit high strength and stiffness and are capable of maintaining these properties at high temperatures. In most composite configurations, the fiber provides the bulk of the strength of the material. Fibers can be grouped into two categories, oxide and nonoxide. Common oxide fibers are made of alumina or silica-based glasses, while most nonoxide fibers are made of silicon carbide or boron nitride.

Non-oxide fibers and matrices, particularly those made of SiC, have found many applications since their development in the early 1980s. They have shown exceptionally high strength at very high temperatures. However, they also have exhibited degradation of strength and stiffness characteristics in applications that involve prolonged exposure to high temperatures and oxidizing environments [15;24;25;43]. Fiber coatings have been developed to help protect the fibers from oxidization [13;16]. However, fiber coatings

themselves tend to break down at high temperatures. Furthermore, fiber coatings add complexity and cost to the manufacturing of CMCs.

Conversely, oxide fibers exhibit an inherent resistance to oxidation. Yet, the mechanical performance of oxide/oxide composites has been less impressive than that of the nonoxide varieties. This difference has been attributed to their different atomic structures. The ionic bonds typical in oxides diffuse easier than the covalent bonds in nonoxides such as SiC. Diffusion leads to increased grain growth and subsequent creep at lower temperatures. Specifically with the use of alumina (Al_2O_3), the oxide of aluminum, competing microstructural components exist. While small grain size is needed for high strength, creep rate is inversely proportional to grain size [27]. Because of their attractive natural oxidation resistance, work continues to develop fibers that maintain their high strength, while also improving the creep rate. The Nextel™ 720 fiber used in this research is one of the latest efforts.

2.2 Fiber/Matrix Interface

As mentioned previously, much of the toughness in CMCs has to do with the interaction between the fiber and matrix specifically at the fiber/matrix interface. The failure of a typical CMC progresses in the following manner. During initial applied loading, fiber and matrix share the stress based on their respective elastic moduli and volume fractions. The first failure will occur in the matrix, which typically has numerous pores and flaws. A network of matrix microcracks will develop. Matrix microcracks eventually coalesce into larger cracks that begin to propagate through the matrix and

6

toward the fiber/matrix interface region. In order to maintain structural integrity of the

fibers, cracks must be deflected around the fibers and not allowed to propagate through

the fiber. A weak fiber/matrix interfacial bond allows debonding and crack deflection

followed by crack bridging, fiber fracture and finally fiber pullout [7:169]. Crack

deflection is the energy dissipating event that provides for a delayed failure and higher

toughness in CMCs. Figure 3 shows a schematic of the failure of a CMC as a function of

the interfacial bond. The interface between fiber and matrix is recognized as being the

critical element that achieves the flaw tolerance that distinguishes CMCs from monolithic

ceramics [36].
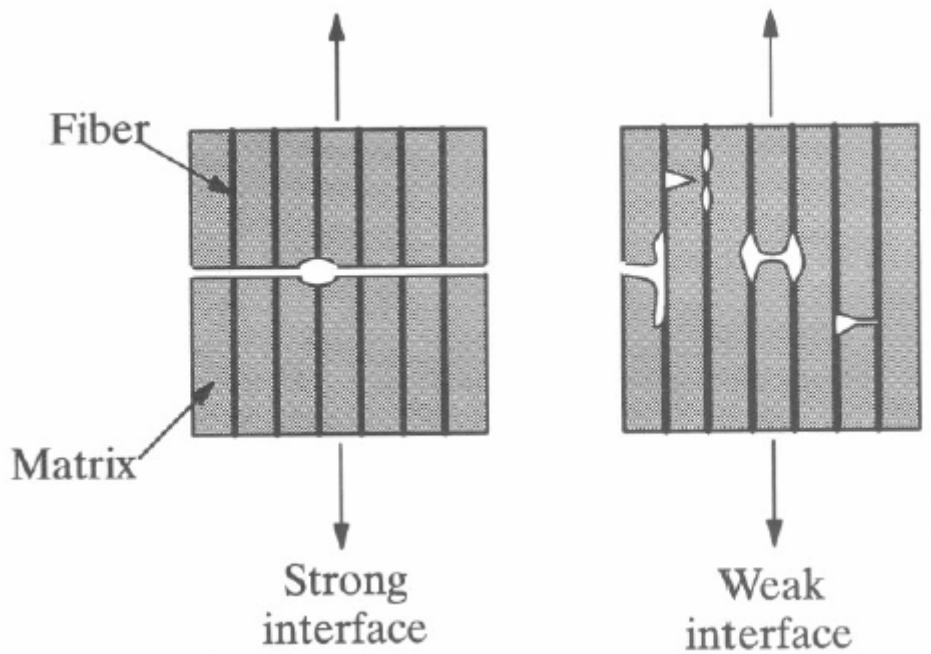
Figure 3. Failure of a CMC as a function of interfacial bond [7:170].

Early ceramic composites relied on a weak interfacial layer serendipitously

formed by the degradation of the fiber. This weak interphase layer protected the fiber

7

from matrix cracks, deflecting them through debonding and sliding, thereby reducing the stress concentration on the fiber [18]. Once the benefits of a weak fiber/matrix interphase were discovered, interphases were specifically designed for use in CMCs and fiber coating was added as a step in the manufacturing process.

Ceramic Matrix Composites that rely on a weak interface for their toughness can be characterized by their stress strain curve. Initially the stress-strain curve is linear, as the matrix and fibers share the load. As microcracks start forming in the matrix, the curve slope starts to decrease. As the cracks in the matrix grow, and then start coalescing, a distinctive knee in the curve is seen. This happens when the cracks propagate through the thickness of the material and all load is transferred to the fibers. At this point the curve is dominated by individual fiber failure and subsequent load transfer to other fibers until the material fails. A typical stress strain curve for a CMC with a weak interface is presented in Figure 4 [20:10].
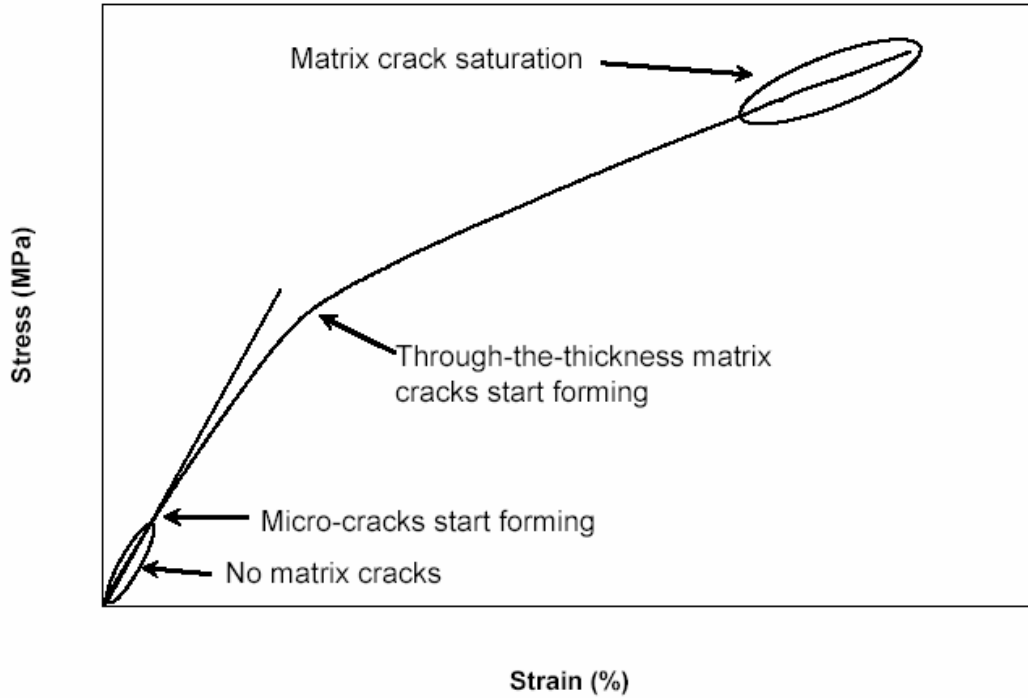
Figure 4. Typical stress strain curve for CMC with weak interface [20:10].

More recently, another method of improving damage tolerance has been developed and used in CMCs. The approach involves using a relatively weak (compared to the fiber), porous matrix [19;37]. The weakness and porosity of the matrix must be controlled so that while it has low enough toughness to enable crack deflection, it exhibits high enough strength to maintain adequate off-axis and interlaminar properties [21]. The different damage processes that enable damage tolerance in CMCs with a weak interface and in CMCs with a porous matrix are shown in Figure 5 [44].
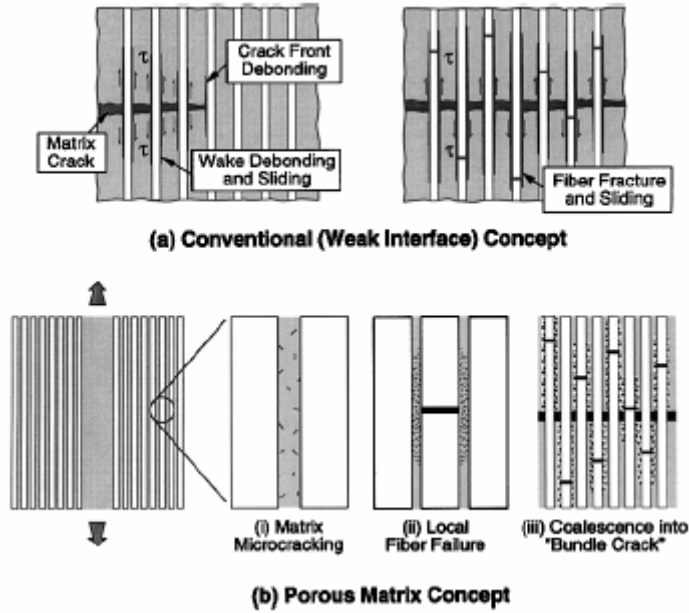
Figure 5. Schematics of the damage processes that enable damage tolerance in (a) conventional dense-matrix weak-interface CFCC and (b) porous matrix CFCC without fiber coatings [44].

Finely distributed porosity in the matrix allows a strong fiber/matrix interfacial bond while at the same time providing energy dissipating mechanisms for the material to possess adequate toughness qualities. While CMCs with weak interfaces have a distinct knee in the stress-strain curve, porous matrix CMCs have a stress-strain curve that remains nearly linear to failure. In this case from the beginning, nearly all of the stress is carried by the high-modulus fibers [12].

The porous matrix allows fibers to be isolated from the cracks in the matrix. Crack fronts are non-continuous in porous materials and crack extension occurs by continued breaking of solid phase units. Fracture occurs by the breaking of grain pairs at grain boundaries. It is this lack of a continuous crack front that keeps the crack fronts in the matrix from propagating through the embedded fibers and provides the energy

dissipation. In this case, fracture of the CMC initiates from the fibers themselves as they break in a stochastically random manner similar to failure of fibers in a fiber bundle not embedded in a matrix [12].

The key to developing a CMC with a porous matrix is to find a range of porosity values that will enable damage tolerance while providing the off-axis strength needed in structural applications. Improvement in off-axis strength by reducing the porosity also reduces the damage tolerance of the material. Studies have shown that a matrix with a high porosity ($\approx$35-40%) exhibits extensive fiber pullout after failure, indicative of random fiber failure, resulting in high strength and fracture toughness. When the matrix density was increased, fiber failures became more correlated, producing more planar fracture surfaces resulting in a dramatic loss in strength and fracture toughness [44].

The use of a porous matrix has a distinct advantage over the weak interface concept, especially when used with oxide fibers and matrix. Fiber coatings introduce cost and complexity in the manufacturing process, are not always stable in oxidizing environments and, thus, can cause composite embrittlement [12].

2.3 Applications of Oxide/Oxide Ceramic Matrix Composites

Numerous applications for CMCs exist in the aerospace field, especially in the field of propulsion. As part of the IHPTET program, discussed in Section 1, CMCs have been demonstrated for use in high-temperature rise combustor liners, turbine vanes, and nozzle flaps [14]. Researchers from EADS have investigated the use of CMC for rocket propulsion. Applications include combustion chambers and nozzle extensions [32].

Significant challenges in using CMCs for these applications were related to the requirement of the composite to have sufficient shear strength for the multiaxis states of stress occurring in propulsion systems.

Oxide/oxide CMCs with a porous matrix are being considered as the candidate materials for use in turbine engine applications. In an effort to improve efficiency in gas turbine engines, increases in turbine inlet temperature (TIT) have pushed the limits of today's superalloys. New materials need to be developed to meet structural needs such as those outlined for the High Speed Civil Transport (HSCT) [26]. These applications will require high strength, excellent creep resistance, and low weight while operating for long periods of time at high temperatures in oxidizing/caustic environments.

In particular oxide/oxide CMCs are being evaluated for applications in combustor walls [27]. Recently, a CMC consisting of N720 fibers and an alumina matrix demonstrated satisfactory performance while subjected to experiments in a combustor test rig. Advanced CFD and FEM analysis techniques were developed to provide better analytical predictions for CMC performance in combustor applications. Analytical predictions will give greater insight into the failure mechanisms of CMCs in the combustor environment. A concurrent effort in (1) optimization of the CMCs and in (2) design of the combustion chamber and components, is expected to accelerate the insertion of the CMCs into aircraft engine application [22;28].

III. Material and Specimens

3.1 Nextel^{TM} 720/Alumina Ceramic Matrix Composite

The continuous fiber ceramic composite used for this research consisted of Nextel™ 720 (N720) fibers in a porous alumina matrix. The N720 fiber is produced by the Minnesota Mining and Manufacturing Company (3M™). The fiber is comprised of ~ 85%Al_2O_3 and 15%SiO_2 in the form of α-alumina (41 vol %) and mullite (59 vol %). The mechanical properties of the N720 fibers are shown in Table 1 [1;41] together with the properties of other oxide fibers developed for load bearing applications.

Table 1. Mechanical properties of N720 and other oxide fibers [1;41].

Property	Nextel™ 720	Nextel™ 610	Nextel™ 650
Composition (wt%)	85Al_2O_3 15SiO_2	>99Al_2O_3	89Al_2O_3 10ZrO_2 1Y_2O_3
Crystal Phases	α-Al_2O_3 + mullite	α-Al_2O_3	α-Al_2O_3 + cubic ZrO_2
Filament Diameter (μm)	10-12	10-12	10-12
Tensile Strength (Gpa)	2.1	3.3	2.5
Modulus (GPa)	260	373	358
Density (g/cc)	3.4	3.9	4.1
Thermal Expansion (ppm/°C)	6.0	7.9	8.0

The microstructure of the N720 fiber is complex consisting primarily of small, elongated grains of α- Al_2O_3 with grains sizes <0.1μm. Additionally, larger mosaic

crystals of mullite and α- Al$_2$O$_3$ with grain sizes up to 0.5μm are present [40]. The absence of non-crystalline phases in the fiber leads to better creep performance [41]. In fact, the N720 fiber had demonstrated better creep performance than any other commercially available polycrystalline oxide fiber (see Figure 6 [40]).
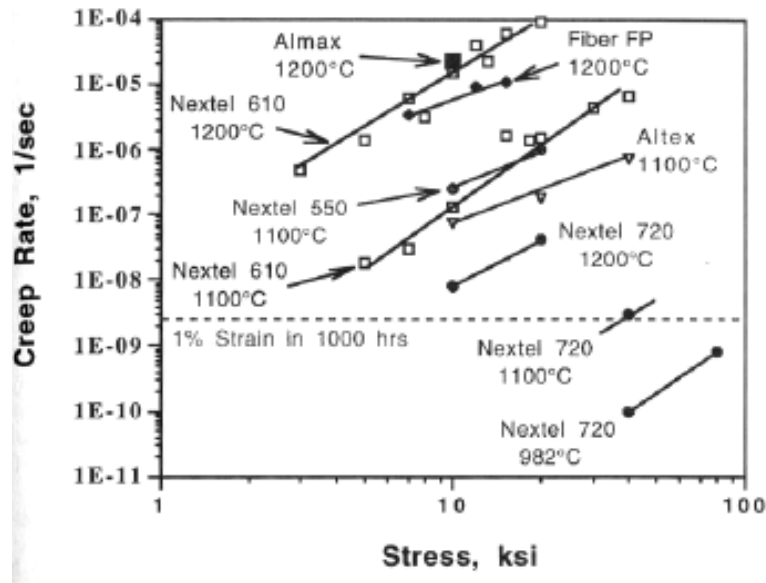
Figure 6. Comparison of creep rates for N720 and other commercially available polycrystalline oxide fibers (10 ksi = 69 MPa) [40].

The N720 fiber combines the high strength of the N610 fiber with lower creep rates. The N610 fiber has an all alumina crystalline structure with a fine, 0.1μm grain size. As mentioned previously, in oxides, creep rate is inversely proportional to grain size [41]. It is the smaller alumina grains that give the N720 fiber strength, while it is the larger mullite grains that slow the creep under load.

The exact methodology for producing the N720 fibers is proprietary, but it involves a sol-gel process. The following steps are common to all sol-gel processing: 1)

formulate sol; 2) concentrate to form a viscous gel; 3) spin the precursor fiber; 4) calcine

to obtain the oxide fiber [7:79].

The CMC used in this research has an all alumina porous matrix. Alumina has

only one thermodynamically stable phase, α-Al$_2$O$_3$. Important properties include a

Young's Modulus of 380 GPa and a coefficient of thermal expansion of 7-8 X10^{-6} /°C.

Also of note is that in its monolithic form, alumina has a rather low fracture toughness of

1-3 MPa•m$^{1/2}$[7:12].

The N720/A CMC used in this research was manufactured by Composite Optics

Inc. (COI) and delivered in the form of 12" X 12" panels. The N720 fibers were woven

in an eight harness satin weave (8HSW). Each panel consisted of a 12 ply (0/90) warp

aligned laminate. The fiber fabric was infiltrated with the matrix in a sol-gel process. A

low temperature and low pressure "vacuum bag" technique was used to dry the material

prior to a pressureless sintering [17]. The properties of the two panels used in this

research, as provide by COI, are given in Table 2.

Table 2. COI N720/A panel properties.

Panel #	Thickness (mm)	Fabric (% Vol)	Matrix (% Vol)	Porosity (%)	Density (g/cc)
3307-1	2.8651	43.8	32.2	24.1	2.77
4569-5	2.6518	47.3	29.4	24.3	2.78

Figure 7 shows an optical micrograph of the as-received N720/A material. The

micrograph shows good matrix infiltration as well as matrix microcracks. Matrix cracks

are formed during the sintering of the material due to a difference in the coefficient of

thermal expansion of the matrix and fiber. These microcracks, however, do not affect the strength of the material because of the porous nature of the matrix [44].

Figure 7. Optical micrograph of polished as-received N720/A material.

3.2 Test Specimen

The specimens were cut from the panels by a local company, Kerf, using a waterjet to specifications in Figure 8. Waterjets use a computer-controlled nozzle that sprays water mixed with garnet particles at high pressures to precision-cut various materials. To reduce fraying at the top edges of the specimens a thin aluminum sheet was placed over the panels during cutting.

After machining, the specimens were cleaned to remove any debris from the waterjet process. Specimens were placed in an ultrasonic bath for 15 m, then soaked in alcohol for 20 m and lastly dried in an oven for 1 h at 250°C.
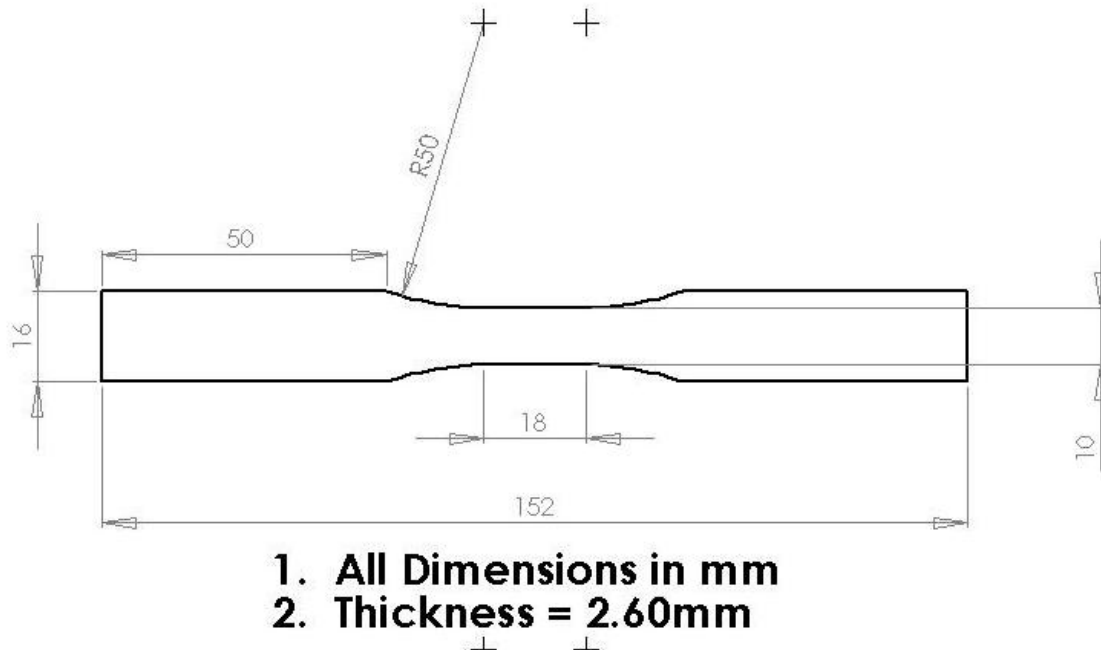
Figure 8. Uniaxial test specimen.

Fiberglass tabs were attached to the grip sections of the specimens with M-Bond 200 adhesive. The tabs protected the surface of the specimen from the rough, surfalloy grips. Figure 9 shows an actual test specimen.
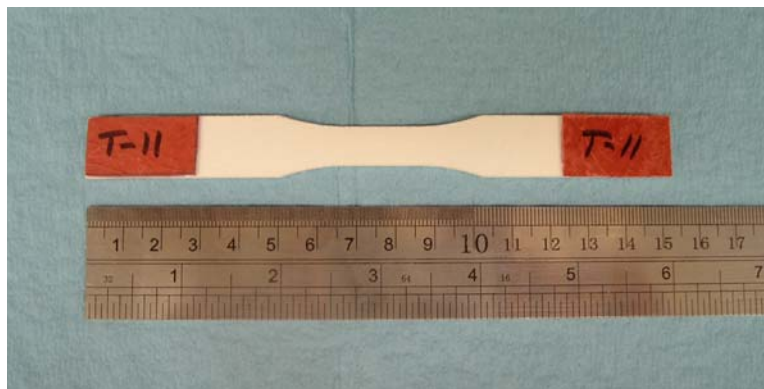
Figure 9. Tabbed test specimen.

IV. Experimental Arrangements and Test Procedures

4.1 Mechanical Testing Equipment

Mechanical testing was conducted on a MTS Systems Corporation model 810 Material Test System servo-hydraulic machine. The load capacity of the unit was 25 kN (5.5 kip). MTS Series 647 hydraulic wedge grips with a Surfalloy surface were used to grip the specimen. A grip pressure of 8 MPa was used in all tests. The grips were water cooled with a Neslab model HX-75 chiller to a temperature of $15^{\circ C}$. A MTS Test Star II controller was used for data acquisition and test control. MTS System Software and Multipurpose Testware (MPT) were used to program and execute the various tests. Figure 10 show the overall mechanical testing station set-up

Figure 10. Mechanical testing station.

A MTS Force Transducer (Model 661.19E-04), with a 25 kN maximum capacity, was used for force measurement. A uniaxial, air-cooled, high-temperature, low contact force MTS Extensometer (Model 632.53E-14) was used for strain measurement. The extensometer was fitted with 6-inch alumina contact rods and protected by a heat shield to maintain operating temperatures within the manufacturers recommended range. Displacement measurement was acquired via a LVDT internal to the MTS servo-hydraulic machine. Figure 11 shows a close-up view of the MTS machine and the extensometer set-up.
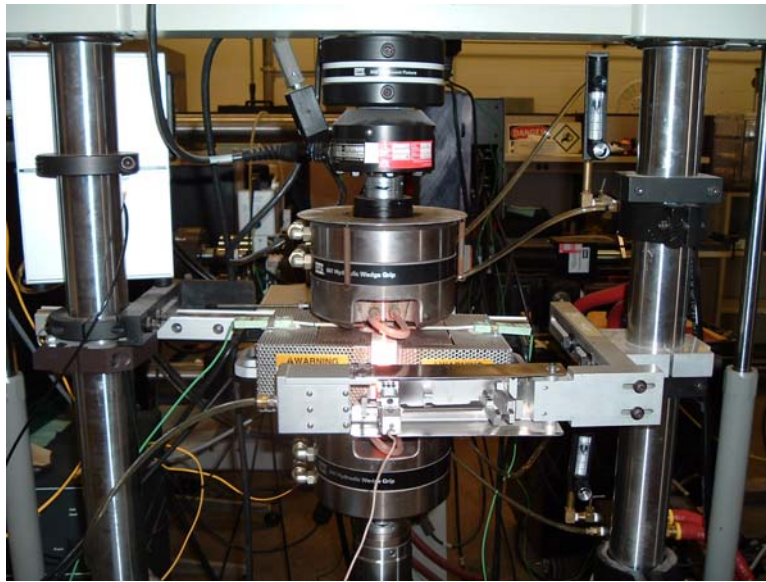
Figure 11. Mechanical testing station close-up.

4.2 Environmental Testing Equipment

To maintain the environment needed for testing, the mechanical testing station was equiped with a furnace, temperature controller and a steam generator.

A compact, two-zone AMTECO Hot-Rail Furnace System was used for all tests. Furnace operation was controlled by a MTS Model 409.83B Temperature Controller. An R-type thermocouple was fitted to each side of the furnace and provided chamber temperature to the controller.

Temperature control was applied as follows. Temperature set-point information was provided from the TestStar II to the temperature controller which applied a PID control algorithm to the elements with a feedback loop from the thermocouples. The temperature controller also provided the thermocouple measurements back to the TestStar II for temperature data recording if desired. It should be noted that this temperature was not the temperature of the specimen, but rather the temperature of the test chambers in the furnace.

A continuous steam environment was provided by an AMTECO HRFS-STMGEN Steam Generation System. Steam was fed to the chamber through a ceramic feeding tube. Deionized water was supplied from a one gallon water reservoir connected to the pump.

An alumina susceptor was used to provide a positive pressure chamber around the specimen forcing out the dry air. This meant that the gage section of the specimen was subjected to a 100% steam environment. The susceptor had two halves that fit around the specimen and inside the test chamber of the furnace. One opening was in the back of the susceptor for the steam feeding tube, and two elongated openings were in the front for the extensometer rods. The susceptor was only used in tests where steam was required. The steam environment could be verified visually during operation by accumulation of condensation on the grips and cooling water lines above the furnace. Figure 12 shows the

susceptor mounted around a specimen in the MTS machine with one of the furnace halves removed.
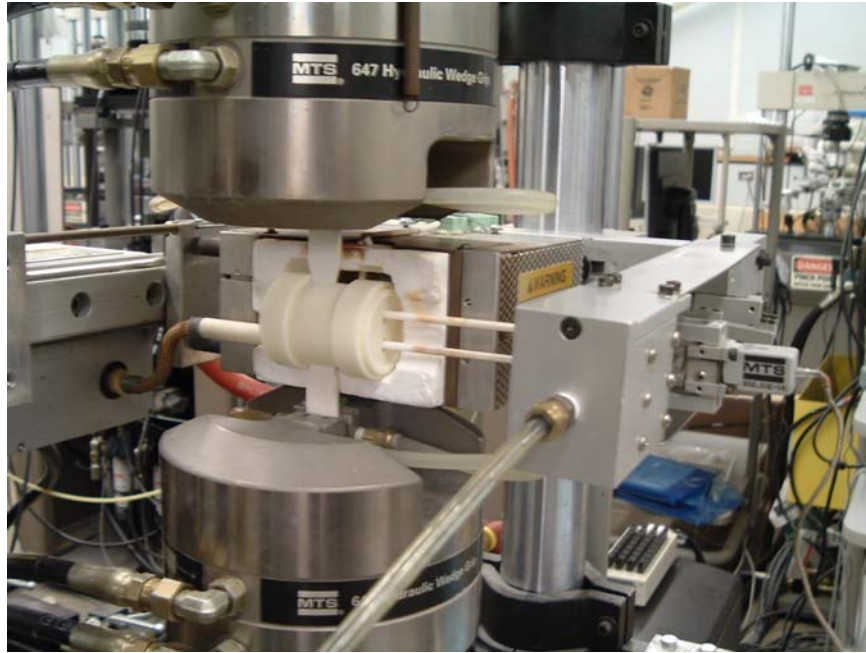
Figure 12. Susceptor mounting arrangement.

4.3 Microstructural Characterization

A Zeiss Dicovery.V12 optical microscope with was used to examine the fracture surface microstructure of each specimen at magnifications of up to 100X. The microscope was equipped with a Zeiss AxioCam HRc digital camera and Axiovision version 4.4 software. This system allowed digital image capturing for comparison of fracture surfaces from different specimens.

An FEI Quanta 200 HV Scanning Electron Microscope (SEM) was used for microstructural characterization of the fracture surface at magnifications of up to

20,000X. The scanning electron microscope differs from an optical microscope in that it doesn't use reflected light to characterize the specimen. Instead, it bombards the specimen with an electron beam and uses special detectors to capture secondary or back-scatter electrons emitted back from the specimen. Unlike a tunneling electron microscope that requires specimens O(1 nm) thick that can be difficult to prepare, an SEM can be used on bulk size specimens. The only limitation is the size of the specimen chamber and stage.

In addition, the SEM included an EDAX Genesis 4000 Energy Dispersive X-Ray Spectroscopy (EDS) system, which used a Sapphire Si(Li) LN cooled EDS detector and Genesis X-ray Microanalysis software for full qualitative and quantitative analysis. Figure 13 shows the SEM and EDS systems.

Figure 13. FEI Scanning Electron Microscope (SEM) and EDAX Energy Dispersive X-ray Analysis Systems (EDS).

4.4 Test Procedures

4.4.1 Mechanical Testing Equipment - Calibration

Prior to the start of the testing program, various parts of the mechanical testing equipment needed to be calibrated. The load cell, grip alignment, and extensometer were calibrated by MTS and AFIT technicians. Next, the MTS controller software was tuned for displacement (stroke) and force control. For displacement control, no specimen was needed, and the gains of the controller were adjusted to match as closely as possible a square waveform and then checked against a saw tooth waveform. For force control, a N720/A specimen was loaded into the machine and the gains of the controller were adjusted to match a square and saw tooth force waveform as closely as possible. The two waveforms were chosen because the saw tooth waveform was representative of the actual testing, and the square wave represented the most difficult waveform for the controller to match.

The furnace temperature controller was calibrated to maintain the desired test temperature of the specimen. One specimen was fitted with two S-type thermocouples. The thermocouples were mounted using a two part Omega CC, High Temperature Cement. After curing for 24 h, they were wrapped with a high temperature wire to ensure contact with the specimen. Care was taken to ensure that the wire did not touch any exposed portion of the thermocouple wire as this would have corrupted the temperature reading. The specimen was mounted into the MTS machine as it would in a typical experiment. The furnace temperature was slowly raised with the MTS System Software until the specimen temperature reached 1200°C. This temperature was held for 8 h to

demonstrate that the temperature controller could maintain stable temperatures within ±

5°C of the nominal. For 1200°C tests in air, the furnace set point was approximately

1060°C. For 1200°C tests in steam, the furnace set point was approximately 1160°C.

The difference is set points can be attributed to the addition of the alumina susceptor and

the continuous flow of the relatively cold (300°C) steam.

4.4.2 Mechanical Test Preparation
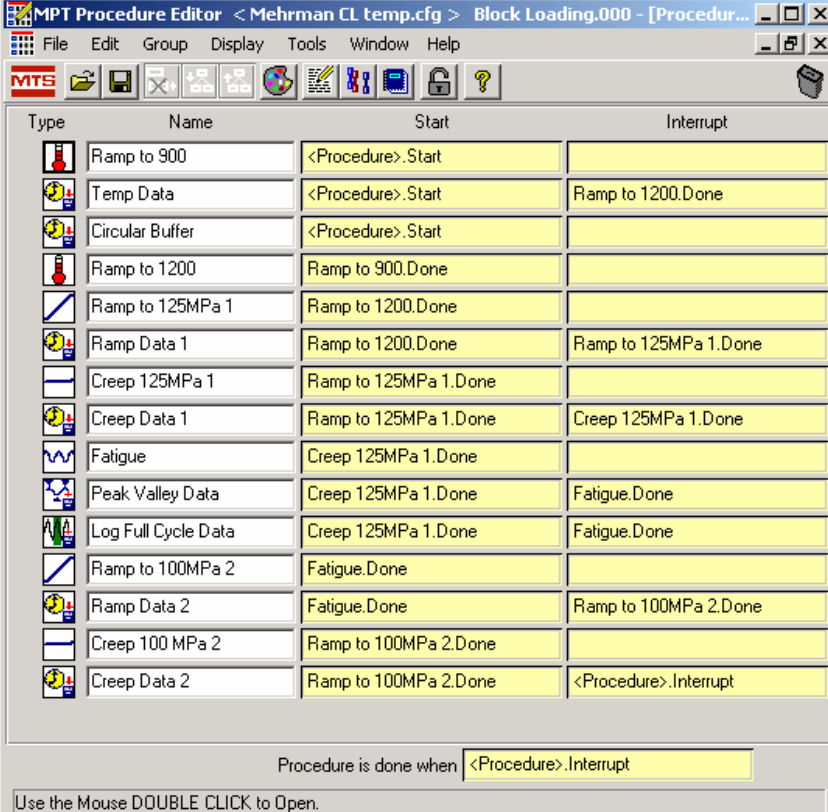
Prior to testing, the servo-hydraulic machine was warmed up. This ensured that

the hydraulic fluid was up to operating temperature and that the gains for the controller

determined in tuning would be accurate. The MTS function generator was used to cycle

the actuator in displacement control mode for at least 15 min. A saw tooth wave with

amplitude of ±0.1 inch was used.

While the hydraulics were warming up, the specimen test section width and

thickness were measured with a Mitutoyo Corporation Digital Micrometer (model

NTD12-6"C). Based on these measurements the cross-sectional area of the test section

was calculated, which was then used to determine the maximum and minimum loads for

the MPT procedure using the following equation:

$$\text{Load} \ = \ \text{Stress x Area} \qquad (1)$$

Next the specimen was placed in the grips. A grip pressure of 8 MPa was used

for all tests. No slipping was observed. The top grip was closed while in displacement

control and the load cell auto-zeroed. Control was switched to force and the bottom grip

was closed. If steam was being used, the susceptor was closed around the specimen and

the oven was pulled forward into position making sure that the steam tube was inserted

into its hole in the back of susceptor. The extensometer was mounted on the specimen.

Then the oven sides were completely closed around the specimen and clearances for the

extensometer rods were checked. The water chiller was turned on and the water

temperature set to 15°C. The water lines for each grip were opened fully and the air

cooling line for the extensometer was opened to 30 psi.

Figure 14. Sample MPT test procedure.

Next the MPT software was opened and the test procedure was written. A sample

test procedure can be seen in Figure 14. Lastly, the test procedure was started and

heating of the specimen began. If steam was used, the steam generator was turned on right after the test started. In all the tests, the furnace temperature was ramped to 900°C in 15 min. Then, the furnace temperature was ramped more slowly (10-15 min) to the desired set point for the test. Lastly, the specimen was allowed to thermally stabilize for 20 min prior to applying the mechanical loading.

4.4.3 Monotonic Tensile Test

Two monotonic tensile tests to failure were conducted for this research. Both were tested in 1200°C laboratory air conditions. The first used stroke control at a constant rate of 0.05 mm/s. Load, strain, displacement and time were measured and recorded every 0.05 s for the duration of the test, which was approximately 10 s.

The second test was conducted in stress (load) control at a constant rate of 0.0025 MPa/s. Load, strain, displacement and time were measured and recorded every 60 s for the duration of the test, which was approximately 20 h.

4.4.4 Combined Creep and Fatigue Testing

Three different test histories combining sustained and cyclic loading were used in this research, and are shown schematically in Figure 15. Maximum stress levels of 125 and 154 MPa were used in tests conducted in laboratory air. Maximum stress levels of 100 and 125 MPa were employed in tests conducted in steam environment.

Test history I consists of cyclic loading with either a 10 or a 100 s hold time at the maximum stress level. The frequency of loading/unloading was 1Hz and the ratio of

minimum stress to maximum stress, R, was 0.05. Thus, the cycle total cycle times were 11 s and 101 s for the 10 s and 100 s hold time tests, respectively. Peak/Valley data was collected for each cycle. In addition, full cycle data was collected for the first 50 cycles, and then gathered at 100, 200, 300, …, 1000, 2000, … cycles. For the full cycles, a two part data collection scheme was used. Data was gathered at 100 N level crossing intervals or every 0.5 s for the 10 s hold time test and every 5 s for the 100 s hold time tests. Run-out was set at 100 h. This is consistent with the desired service life for the material.

Test history II was a block loading sequence consisting of 10^5 fatigue cycles followed by a creep test. Run-out was defined as survival of 100 h of creep. Fatigue cycles were conducted with the frequency of 1 Hz and a ratio of minimum to maximum stress, R=0.05. A data point was collected at the peak and valley of every fatigue cycle. In addition, full cycle data were collected every 0.05 s, the same cycle numbers as in test history I. During the creep block of the test, data was collected every 30 s.

Test history III was a block loading sequence consisting of a creep test, followed by test history II. Duration of the initial creep test was 2 h for tests conducted in laboratory air and 0.75 h for tests conducted in steam environment. Run-out for this test profile was defined as survival of 100 h at creep stress during the second creep period. Data acquisition was carried out as described for test history II.

All specimens that achieved a run-out were subjected to a tensile test to failure to determine the retained strength.
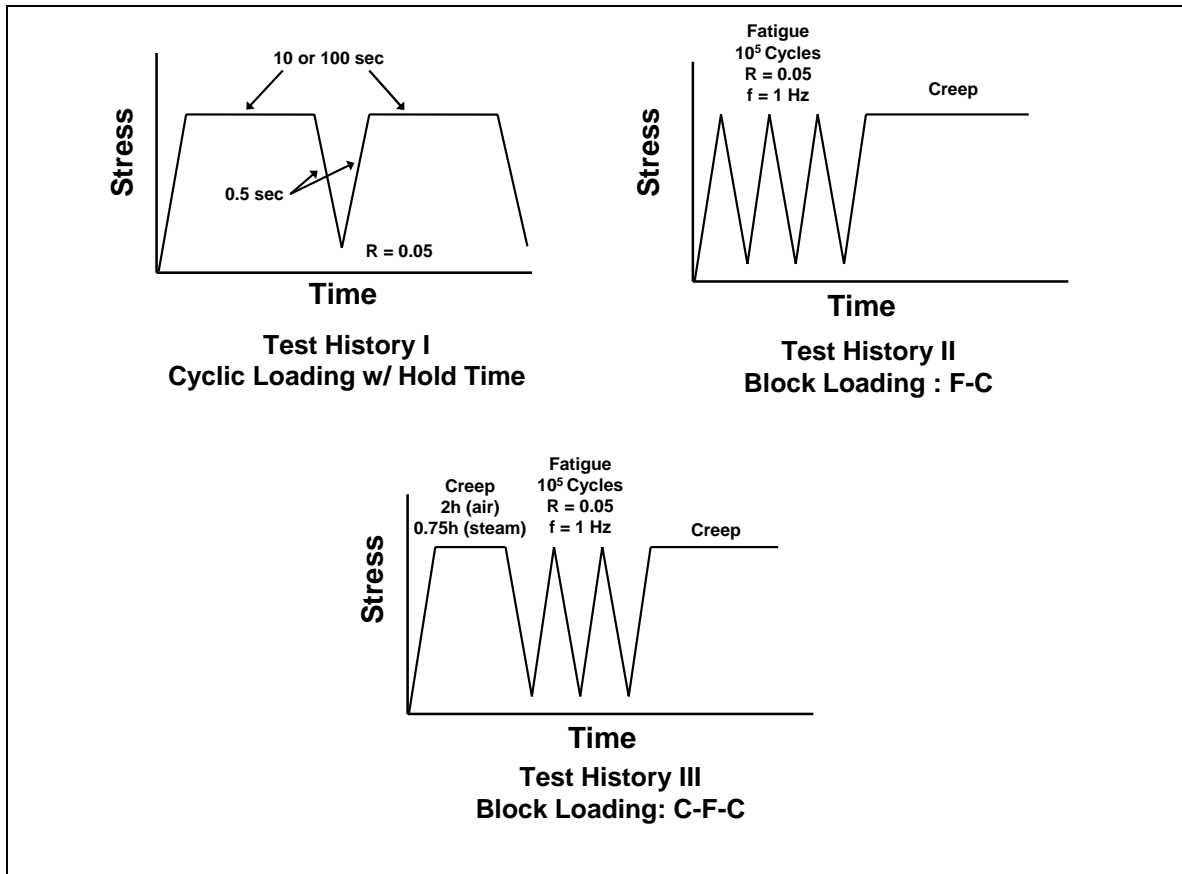
Figure 15. Combined creep/fatigue test histories.

4.4.5 Microstructural Characterization

Post-test microstructure was first examined with the optical microscope. A magnification of 9.7X was used to examine the entire surface across the width of the fractured test section. In addition, a magnification of 15X was used to examine the fracture surface across the thickness of the fractured test section. Digital pictures were taken of each half of the failed specimens for documentation.

After observations by the optical microscope, the specimens were prepared for examination with the SEM. One half of the failed specimen was selected and the fracture surface was cut off with a Sherline Model 5410 diamond saw. The cut was made ~2mm

behind the damage zone of the specimen. The fracture surface was then mounted onto a 12.4mm SEM specimen stage with carbon paint.

Non-conductive materials like the alumina and mullite found in the Nextel 720/A CMC tend to build up a charge when bombarded by the electron beam of the SEM. This leads to distortion of the image and, if severe enough, can lead to damage of the specimen. To combat this problem, two different methods were used. The first was to coat a specimen with a thin layer of a conductive material. For this research, both carbon and gold coatings were tried out. Carbon coating was chosen based on image quality, and more importantly, because gold would have been detrimental to the spectroscopy characterization discussed later. A SPI Supplies SPI-Module Control and Carbon Coater, shown in Figure 16, were used to coat the specimens.

Figure 16. SPI-Module Controller and Carbon Coater.

The second approach taken to reduce charging of the specimens was to use the Environmental Scanning Electron Microscope (ESEM[TM]) mode of the SEM. The ESEM is a low-vacuum mode of the SEM that utilizes water vapor pumped into the test chamber and a special Gaseous Secondary Electron Detector (GSED). The water vapor serves two purposes: (1) it acts as a cascade amplifier for the secondary electrons that are emitted from the specimen, by releasing secondary electrons of their own, and (2) the now positively charged water vapor molecules neutralize the negative charge on the non-conductive specimen [2]. Therefore, the ESEM mode permits observation of uncoated specimen. The downside to this mode is that the image quality is not as good as that obtained for specimens coated with a conductive material. Maximum resolutions of only 3000X were obtainable.

Every specimen was examined in ESEM mode and digital photos were taken at various magnifications ranging from 50X to 3000X. Only a few of the specimens were coated with carbon and observed at higher magnifications in high vacuum mode. Figure 17 shows two specimens prepared for examination in the SEM. The specimen on the left is uncoated and the specimen on the right is carbon coated.

Figure 17. Specimens prepared for SEM. Uncoated specimen on left, carbon coated specimen on right.

For EDS analysis, the high vacuum mode of the SEM must be used. The water vapor used in the ESEM mode of the SEM interfered with the X-ray detector sampling. Therefore, the specimens characterized by EDS analysis were coated with carbon.

Untested N720/A CMC was mounted in a carbon resin fill and polished for viewing with the optical microscope as well as the SEM. A Buehler Simplimet 2000 automatic mounting press was used to mount the specimen in a Buehler Konductomet conductive filled phenolic mounting compound. The specimen was then polished with a Buehler PowerPro 5000 variable speed grinder and polisher. The specimen was first ground with 240(60 μm) , 400(30 μm), and then 600(15 μm) grit sandpapers. Then it was polished with 6μm, 1μm, 0.1μm, and lastly 0.05μm Buehler Metadi diamond suspension paste. Lastly, it was carbon coated using the SPI Supplies SPI-Module Control and Carbon Coater mentioned above. Figure 18 shows a picture of the mounted and polished specimen prior to carbon coating.

Figure 18. Mounted and polished N720/A specimen.

V. Results and Discussion

The tests carried out during this investigation are summarized in Table 3, where specimen number, panel number, test type and test environment are given together with the maximum stress level for each test.

Table 3. Test Matrix.

Specimen Number	Panel Number	Test Type	Test Environment	Maximum Stress (MPa)
T-5	3307-1	Monotonic, Disp. Rate	Laboratory Air	186
T-6	3307-1	Cyclic, 10s Hold Time	Laboratory Air	100
T-7	3307-1	Cyclic, 10s Hold Time	100% Steam	100
T-8	3307-1	Cyclic, 10s Hold Time	Laboratory Air	125
T-9	3307-1	Cyclic, 100s Hold Time	100% Steam	100
T-10	4569-5	Cyclic, 100s Hold Time	Laboratory Air	125
T-11	4569-5	Cyclic, 100s Hold Time	Laboratory Air	125
HT-12	3307-1	Monotonic, Load Rate	Laboratory Air	182
T-13	4569-5	Block: F-C	Laboratory Air	125
T-14	4569-5	Cyclic, 10s Hold Time	Laboratory Air	154
T-15	4569-5	Block: F-C	100% Steam	100
T-16	4569-5	Cyclic, 10s Hold Time	100% Steam	125
T-17	4569-5	Cyclic, 100s Hold Time	Laboratory Air	154
T-18	4569-5	Cyclic, 100s Hold Time	100% Steam	125
T-19	4569-5	Block: F-C	Laboratory Air	154
T-20	4569-5	Block: F-C	100% Steam	125
T-21	4569-5	Block: C-F-C	Laboratory Air	125
T-22	4569-5	Block: C-F-C	100% Steam	100
T-23	4569-5	Block: F-C	100% Steam	125
T-24	4569-5	Cyclic, 10s Hold Time	100% Steam	100
T-25	4569-5	Cyclic, 100s Hold Time	100% Steam	100
T-26	4569-5	Block: C-F-C	Laboratory Air	125
T-27	4569-5	Block: F-C	100% Steam	125
T-28	4569-5	Block: C-F-C	100% Steam	100
T-29	4569-5	Creep	Laboratory Air	125
T-30	4569-5	Cyclic 10s, Hold time	Laboratory Air	125

5.1 Monotonic Tensile Tests

5.1.1 Displacement Controlled Test

A monotonic tension test to failure (specimen T-5) was conducted at 1200°C in laboratory air in displacement control at a rate of 0.05 mm/s. Elastic modulus, E, ultimate tensile strength, UTS, and failure strain obtained in this test are presented in Table 4 together with the tensile properties obtained in earlier investigations.

Table 4. Elastic modulus, ultimate tensile strength and failure strain of a N720/A CMC at 1200°C.

Data Source	Elastic Modulus (GPa)	Ultimate Tensile Strength (MPa)	Failure Strain (%)
Current effort	77.7	186.0	0.37
Harlan[11;29], Eber[10;29]	74.7	192.2	0.38
COI [8]	76.1	218.7	0.43

The stress-strain curve obtained in this test is shown in Figure 19 together with the stress-strain curve reported in ref [10;11;29]. It is seen that the results are consistent with those reported previously. Note the linearity of the stress strain curve, which is consistent for a CMC with a porous matrix. In this case the fibers carry most of the load, the stress-strain behavior of the composite is fiber-dominated [12].
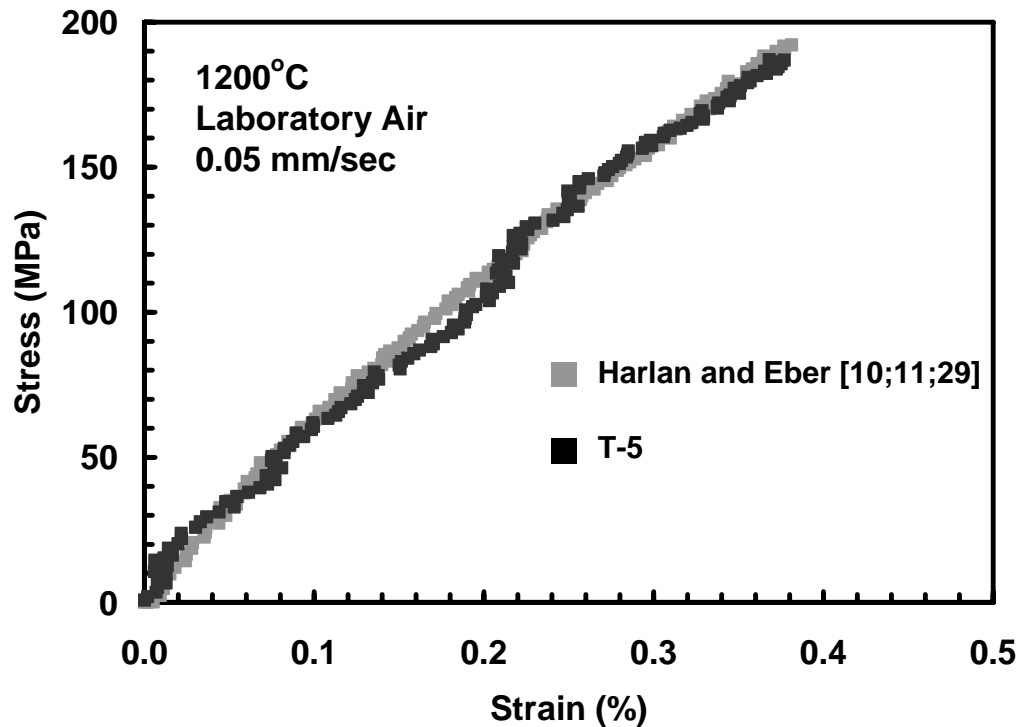
Figure 19. Tensile stress-strain curves for N720/A at 1200°C in laboratory air.

5.1.2 Load Controlled Tests

A preliminary investigation of the effect of load rate on the stress-strain behavior and properties of N720/A at 1200°C was carried out by Z.T. Kier [30]. One surprising result of his research was that while loaded at low stress rate, the material first exhibited decreasing strain followed by increasing strain. The two tests conducted at a stress rate of 0.0025 MPa/s produced the same result. One possible explanation was that the material had not been sintered long enough during fabrication and was continuing to sinter during the initial portion of the test causing shrinking of the fiber and consequently a decreasing strain. To test this theory, a specimen, HT-12, was sintered at 1200°C for ~12 h and subsequently tested under the same conditions. The stress strain curves

obtained in this test are shown in Figure 20 together with the stress-strain curves produced by Z.T. Kier [30].
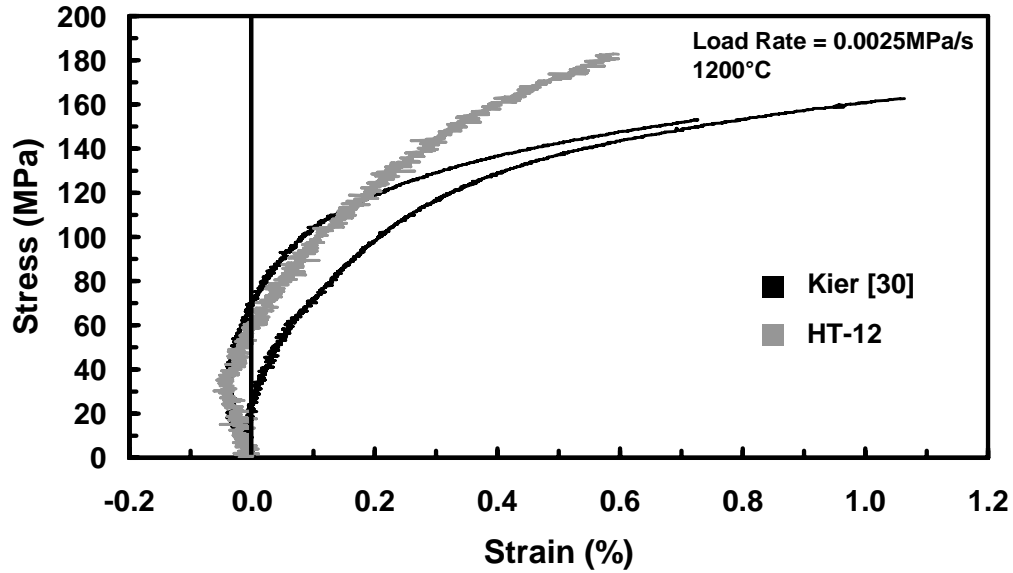
Figure 20. Monotonic stress-strain curve for N720/A tested at load rate of 0.0025 MPa/s at 1200°C in laboratory air. Kier data provided by ref [30].

It is seen that additional sintering of the material did not change the stress-strain response. Further, it was found that negative creep strains were observed by Wilson et al. [40] during creep tests of individual N720 fibers at 1093°C at stress levels below 138 MPa. Creep strain is accumulated at zero load rate. Given that the response of N720/A is fiber-dominated; decreasing strain at low load rates and low stress levels may be due to the same mechanisms as the negative creep strain reported by Wilson for the N720 fibers. Wilson offered that the shrinkage of the fibers "resulted from the crystallization of α-Al_2O_3 from mullite supersaturated with alumina."[40:1011]

5.2 Combined Creep-Fatigue Tests in Laboratory Air Environment

Twelve combined creep-fatigue tests were conducted at 1200°C in laboratory air. The results are summarized in Table 5. For Block loading tests, the time to failure is reported by noting the time at each portion of the block with a "+" in between if the specimen continued to the next portion. For example, specimen T-21 survived 2 h of creep followed by 27.7 h of intermediate fatigue followed by 15.1 h of additional creep prior to failure. The results are consistent with those previously reported [10;11;29]. The only discrepancy noted was in a 125 MPa creep test. To resolve the discrepancy an additional creep test was conducted at 125 MPa.

Table 5. Summary of N720/A test results obtained at 1200°C in laboratory air.

Specimen	Test Type	Max Stress (MPa)	Cycles to Failure	Time to Failure (h)	Strain at Failure (%)
T-6	Cyclic, 10s Hold	100	>47059	>144	Run-out
T-8	Cyclic, 10s Hold	125	5587	17.1	0.94
T-30	Cyclic, 10s Hold	125	12451	38.1	1.36
T-10	Cyclic, 100s Hold	125	>4571	>128	Run-out
T-11	Cyclic, 100s Hold	125	>4003	>113	Run-out
T-13	Block: F-C	125	N/A	27.7 + >101	Run-out
T-21	Block: C-F-C	125	N/A	2 + 27.7 + 15.1	1.12
T-26	Block: C-F-C	125	N/A	2 + 27.7 + 13.2	1.23
T-29	Creep	125	N/A	18.1	1.50
T-14	Cyclic, 10s Hold	154	5759	17.6	0.74
T-17	Cyclic, 100s Hold	154	98	2.73	0.86
T-19	Block: F-C	154	N/A	27.7 + 1.68	0.92

Note that the cyclic test with a hold time of 100 s and maximum stress of 125 MPa was repeated. The initial test was interrupted due to a furnace malfunction and

restarted after the furnace was repaired. The test was repeated to remove any doubt about

the validity of the initial test results. Figure 21 shows the variation with time of

maximum and minimum strain and it is seen that the results of both tests were consistent.

Ratcheting was observed in all tests which is consistent with results reported by Eber

[10;29]. Further figures in this report will focus on maximum strain and no longer show

the strains at minimum stress.
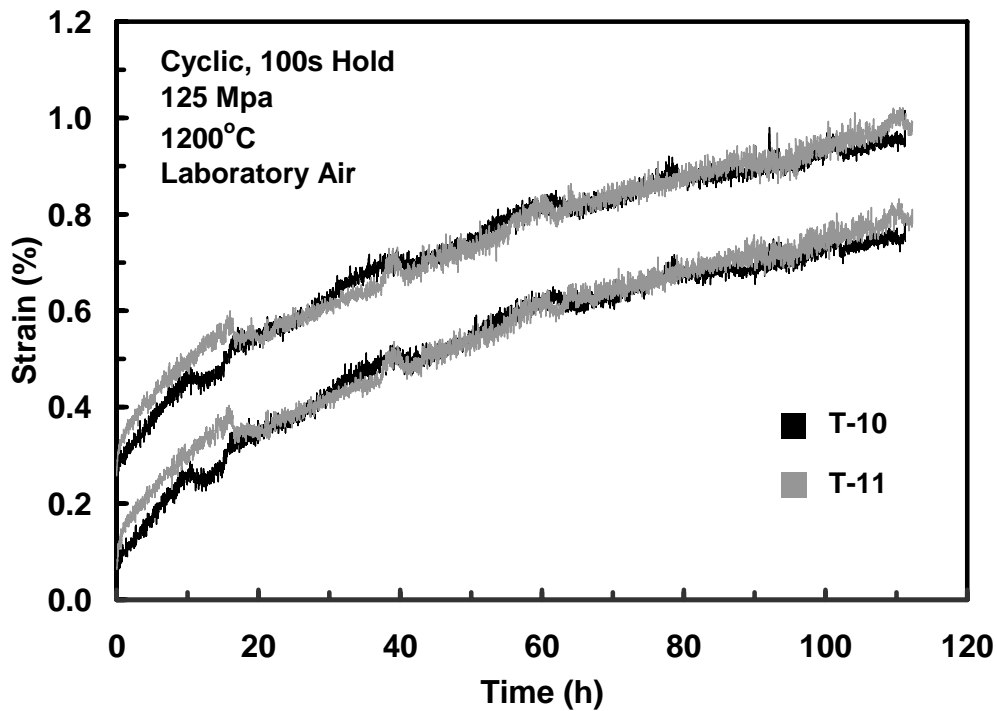
**Figure 21. Maximum and minimum strain vs time for N720/A composite tested with
cyclic, 100s hold condition at 125MPa and 1200°C in laboratory air.**

5.2.1 Cyclic Tests with Hold Time

Table 6 summarizes the results obtained by Harlan [11;29] and Eber [10;29] for

N720/A at 1200°C in laboratory air in creep and fatigue tests respectively. These results

represented the outer bounds of the cycle times investigated in this research, with creep

being viewed as static fatigue. It is clear from these results that the fatigue performance

of N720/A is very good, with run-out of 10^5 cycles being achieved at maximum stress

levels up to 90% of the UTS. The creep performance, however, shows a need for

improvement. Run-out of 100h of creep has been used for this material. This run-out

condition was arrived at by considering the expected application in the aerospace

industry. The run-out was only achieved at stress levels below 50% of the UTS. In

addition, a study by Milz et al. showed that the fracture behavior of the N720 fiber is

controlled by creep damage [23]. It was reasonable to conclude from these results that it

was the time at maximum stress that caused the most damage to the material, and that

longer hold times should have lower time to failure.

Table 6. Summary of creep[11;29] and fatigue[10;29] test results for N720/A at 1200°C in laboratory air.

Data Source	Test Type	Max Stress (MPa)	Cycles to Failure	Time to Failure (h)	Strain at Failure (%)
Harlan[11;29]	Creep	80	N/A	255	1.11
Harlan	Creep	100	N/A	41.0	3.04
Harlan	Creep	125	N/A	4.25	3.40
Harlan	Creep	154	N/A	0.27	0.58
Eber[10;29]	Fatigue	100	>120199	>33.4	Run-out
Eber	Fatigue	125	>146392	>40.7	Run-out
Eber	Fatigue	150	>167473	>46.5	Run-out
Eber	Fatigue	170	>109436	>30.4	Run-out

Figure 22 shows the results of the cyclic tests with hold-times in laboratory

together with the results produced by Harlan [11;29] and Eber [10;29]. As expected, the

lowest times to failure are observed in creep and the longest in fatigue. At 154 MPa, the

10 s hold time test showed an order of magnitude improvement over the 100 s hold time test, which exhibited an order of magnitude improvement compared to the pure creep test.
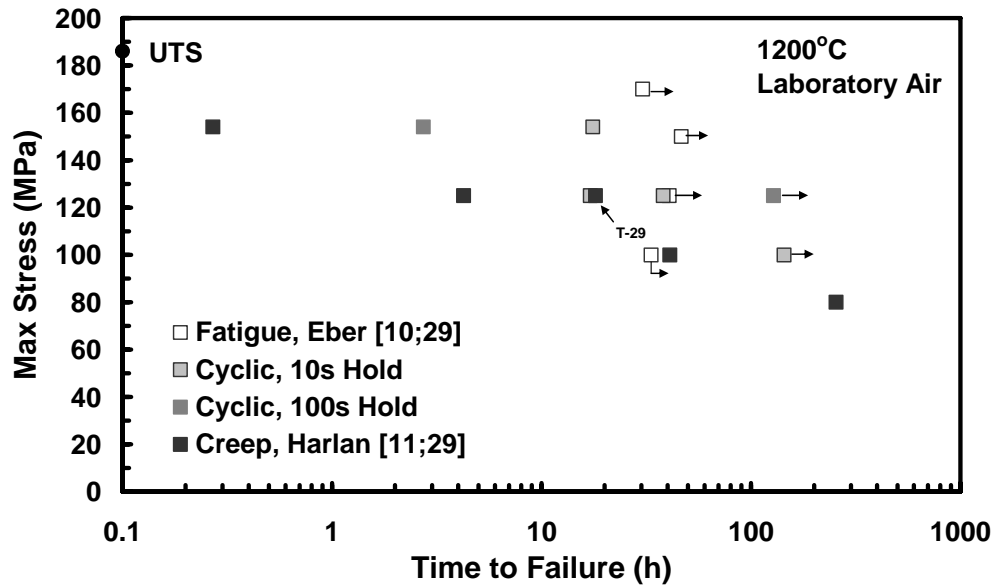
Figure 22. Maximum stress vs time to failure for N720/A at 1200°C in laboratory air. Creep[11;29] and fatigue[10;29] are also shown.

Tests conducted at the maximum stress of 125 MPa showed somewhat different results. While the 100 s hold time test achieved a run-out, the first 10 s hold time test (specimen T-8) failed after ~ 17 h. Furthermore, the 10 s hold time tests at 125 MPa performed slightly worse than the 10 s hold time test at 154 MPa (specimen T-14) with about the same time to failure and higher strain accumulation. The 10 s hold time test at 125 MPa was repeated. Results of the three tests are presented in Figure 23. The repeated test (specimen T-30) did not proceed as planned due to a temperature controller malfunction. The test was interrupted after 21 h of testing, at which point the specimen was held at 125 MPa for 0.5 h. At this point (labeled A in Figure 23) the cyclic test with

10 s hold time was resumed and continued until failure. The total test duration from start to failure was 38.1 h. It is not known how the additional creep time at 125 MPa affected the time to failure of this specimen. However, two points should be noted: (1) after the interruption and restart, the strain returned to the same, pre-interruption level, and continued at the same strain rate to failure, and (2) the strain accumulated by T-30 is nearly the same as that accumulated by T-8, and significantly greater than the strain accumulated by T-14 tested at a higher stress level of 154 MPa.
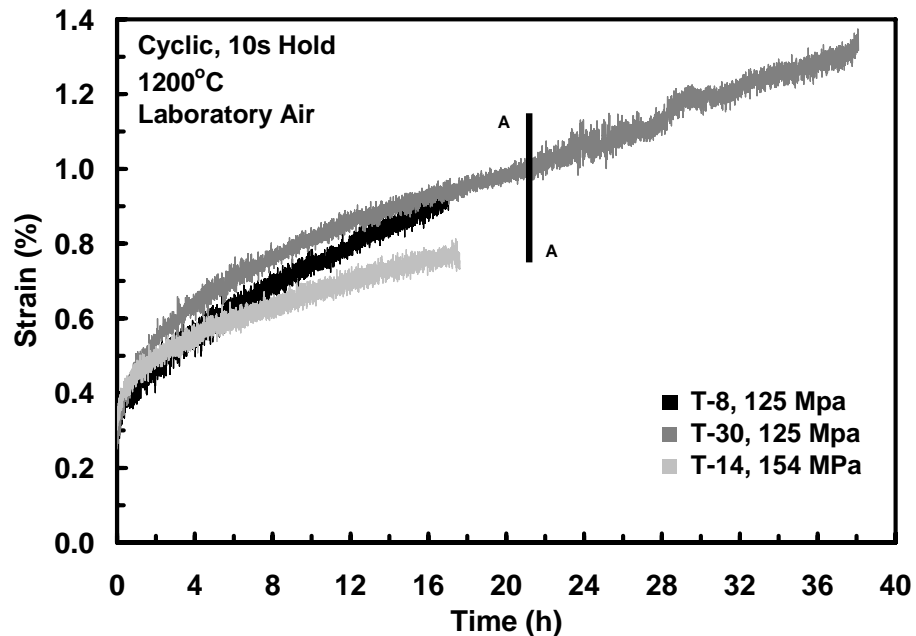
Figure 23. Maximum strain as a function of time at 1200°C in laboratory air.

Another way to look at the cyclic data is to examine how quickly strain accumulates. In all of the tests, there was an initial transient rise in maximum strain levels that slowed to a point where strain continued to accumulate at a steady rate. Figure 24 shows the accumulation of strain at the maximum stress level versus time for the 125MPa (a) and 154 MPa (b) load levels for each of the cyclic test conditions. The strain

measurement was taken at the maximum stress level and does not include the thermal or elastic strains, thus all of the strains start at zero.
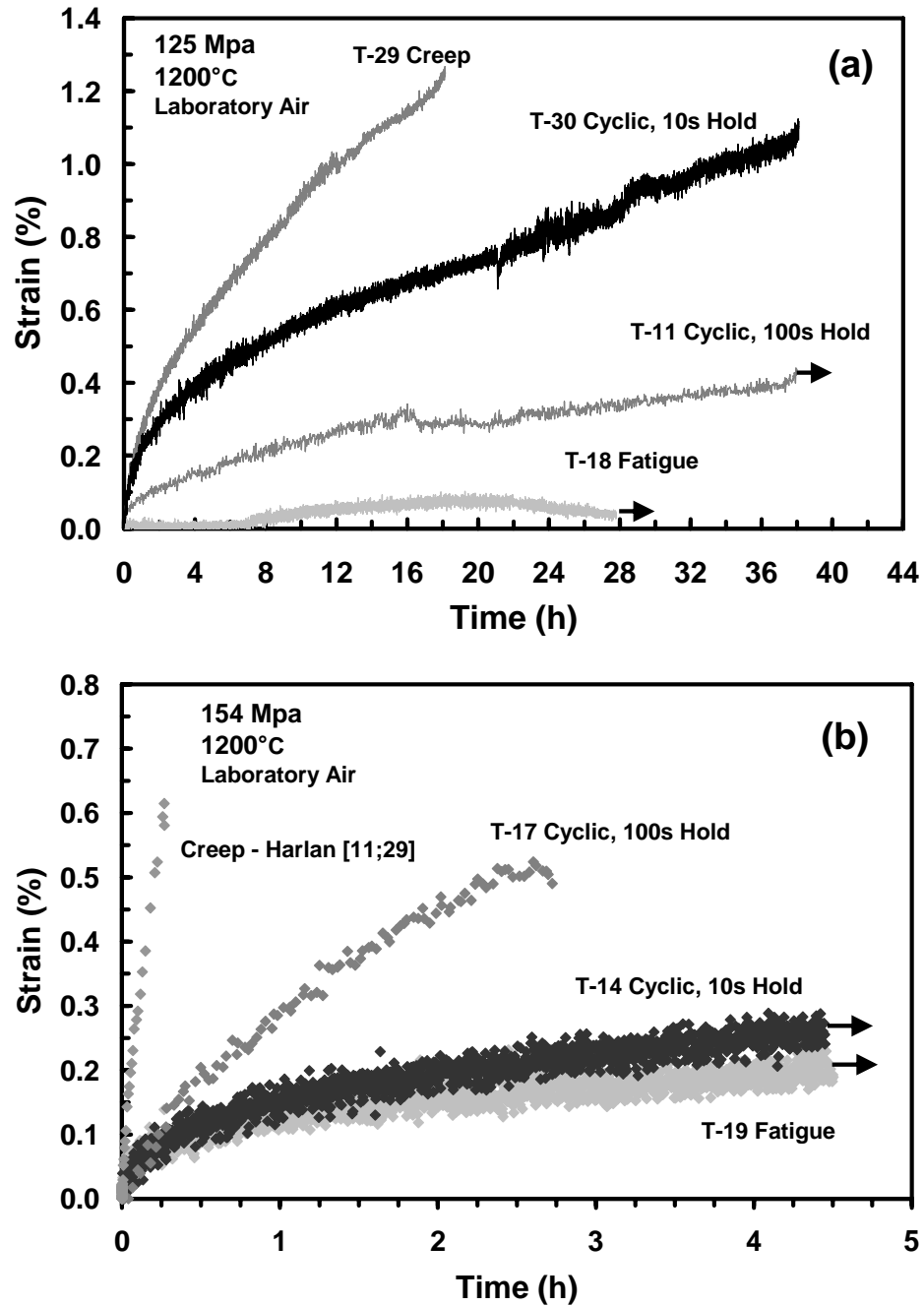
Figure 24. Maximum strain as a function of time at 1200°C in laboratory air for maximum stress of (a) 125 MPa and (b) 154 MPa. Creep data from ref [11;29] included.

Using the graphs of maximum strain as a function of time, the steady-state strain rate (i.e. the rate of change of maximum strain with time) was calculated for each of the tests represented in Figure 25. Steady state strain rate is an indicator of how damaging is the particular type of loading. Figure X shows the strain rate versus maximum stress for the cyclic loading conditions. It should be noted that the fatigue strain rates presented are those obtained from the fatigue portion of the Block loading: F-C tests, at maximum stress levels of 125MPa (specimen T-13) and 154MPa (specimen T-19). As expected, the longer the time spent at maximum load, the higher the strain rate, resulting in more rapid damage development and earlier failure. This is consistent with results reported by Zawada and Lee for a N610/AS composite [42]. The only exception once again was the cyclic, 10 s hold time test at 125 MPa.
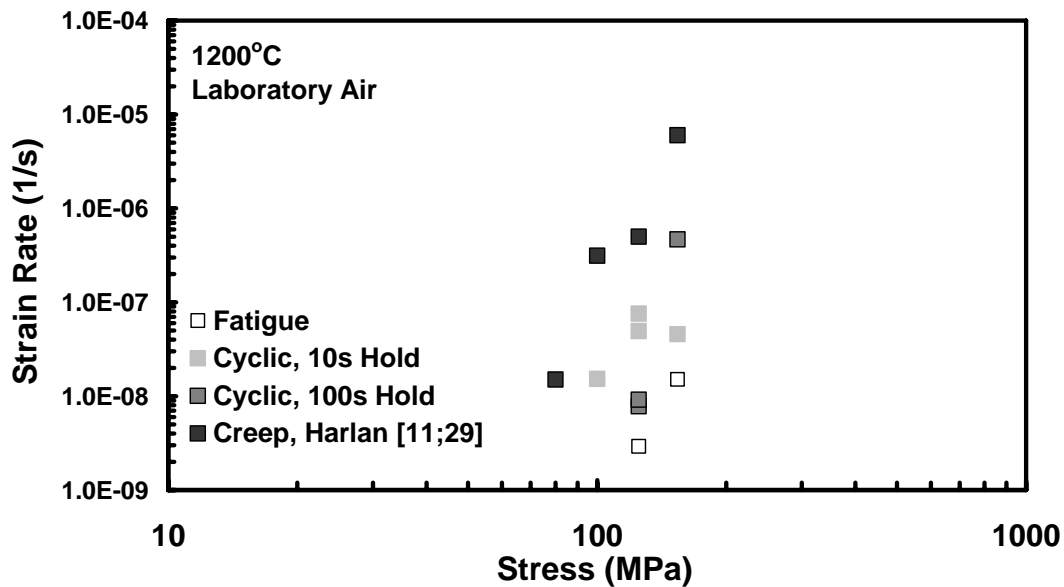
Figure 25. Strain rate as a function of maximum applied stress at 1200°C in laboratory air. Creep data from [11;29] are also shown.
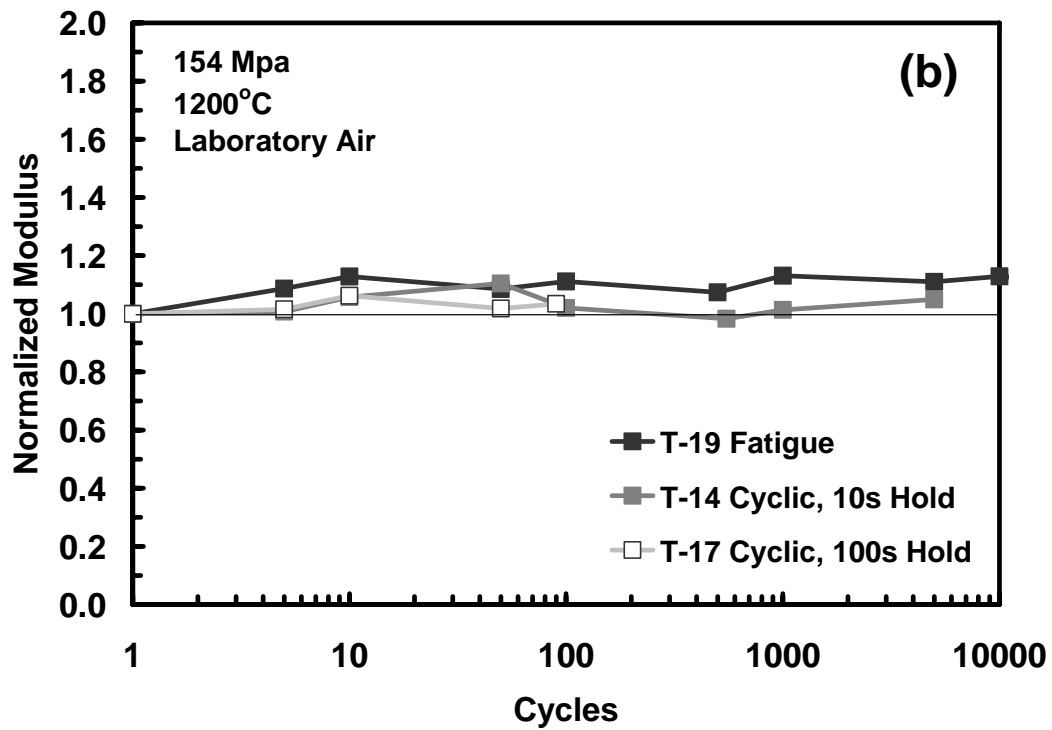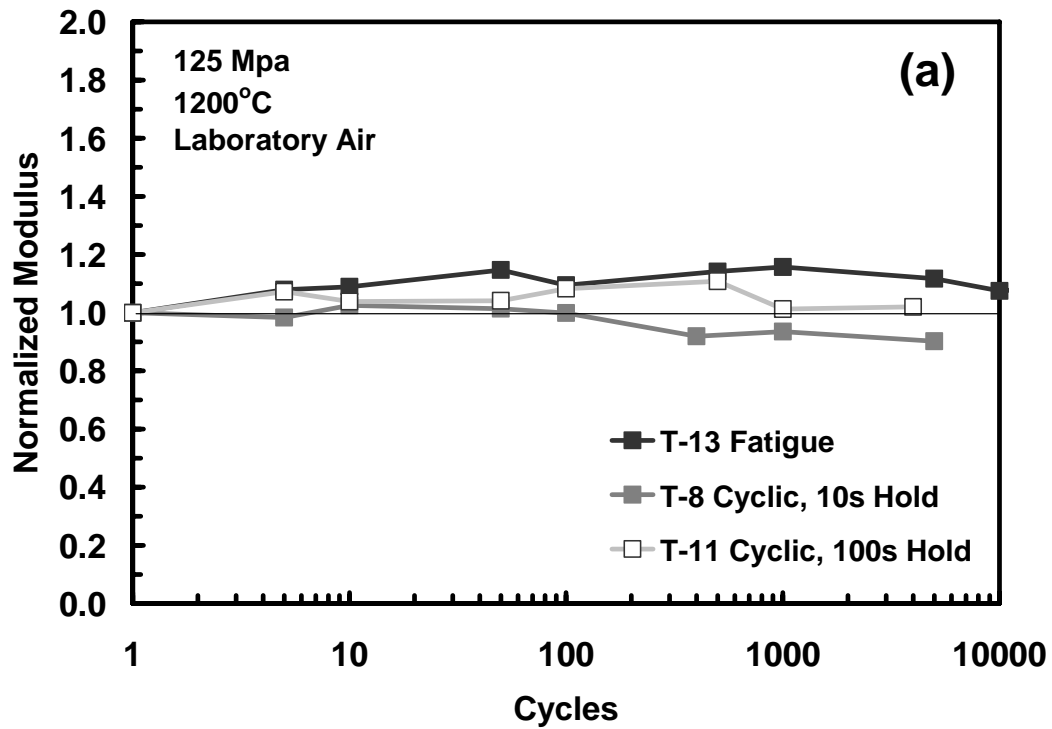
Figure 26. Normalized modulus versus cycles at 1200°C in laboratory air environment for maximum applied stress of (a) 125 MPa and (b) 154 MPa.

To further investigate the influence of hold times on fatigue, the evolution of modulus versus cycle was compared for the cyclic tests with and without hold times. Increases in the modulus over time indicate cyclic hardening of the material. A secant modulus was calculated, taking the slope of the stress strain curve for the particular cycle from the minimum to maximum stress. The data was then normalized to the modulus of the first cycle. Results for maximum stress levels of 125 MPa and 154 MPa are shown in Figure 26. The modulus does not fluctuate appreciably, staying within ±20% of the initial value. In general, the modulus increases at first and then returns slowly toward the initial modulus. The one instance where it doesn't follow that trend is, once again, the cyclic, 10 s hold time test at 125MPa.

5.2.2 Influence of Prior and Intermediate Fatigue Cycling on Creep Response in Laboratory Air

Previous studies have shown a large difference in the time to failure under creep and fatigue loading, with fatigue tests achieving run-out of 10^5 cycles in testing up to 170 MPa in air (~90% of UTS). Block loading test were conducted to study the effects of prior and intermediate fatigue on the creep performance of the material. In the laboratory air tests, the intermediate fatigue cycling was introduced after 2 h of creep, or near the end of the primary creep regime of the material. The results of the block loading profiles are shown in Figure 27.
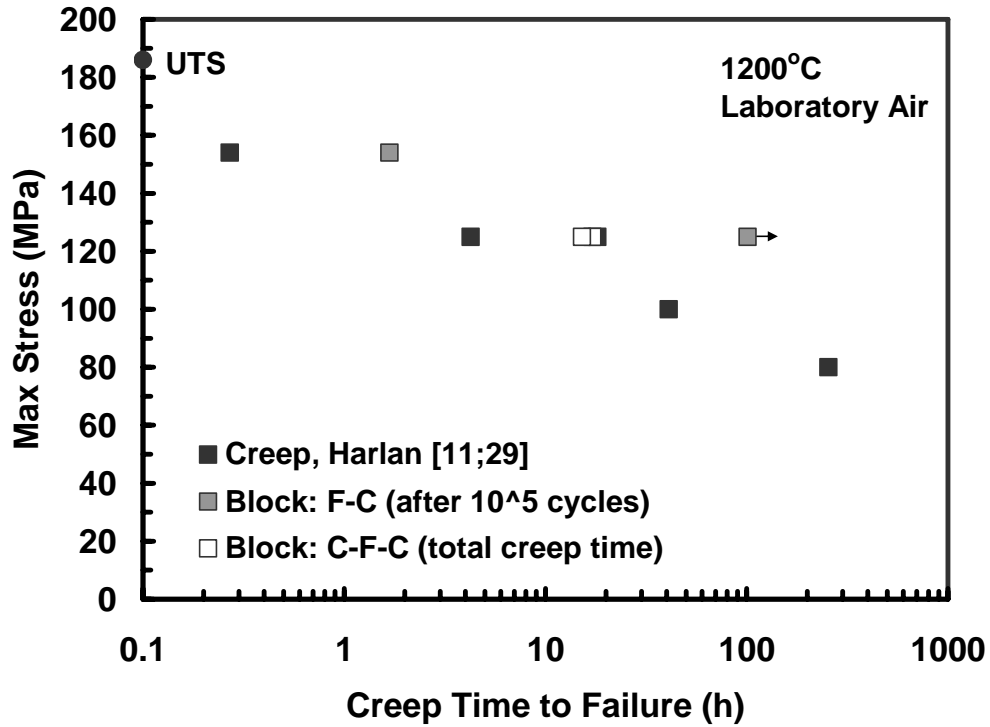
Figure 27. Maximum stress vs creep time to failure of N720/A at 1200°C in laboratory air. Creep data from ref [11;29] included.

Prior fatigue cycling improved the creep life of the material at both the 125 MPa and 154MPa stress levels by an order of magnitude. It appears that fatigue "strengthens" the material. This result is supported by the findings reported by Eber [10;29], namely that the retained strength of the N720/A specimens that had achieved run-out in fatigue was higher than the UTS of the untested material. Further insight can be gained by examining the strain accumulation with time, shown in Figure 28. Much lower creep strains were accumulated in both the 125MPa and 154 MPa tests subjected to prior fatigue.
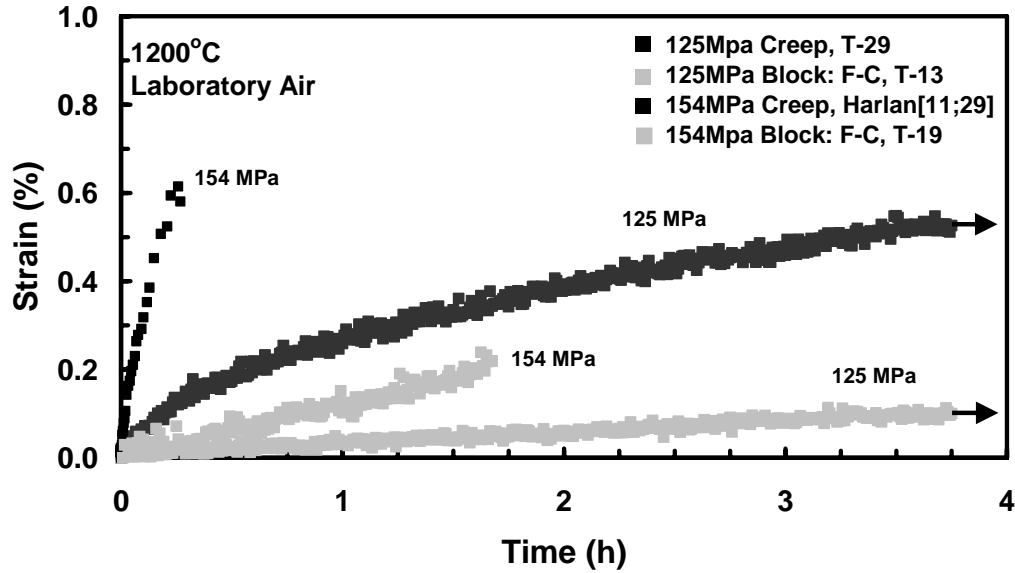
Figure 28. Creep strain as a function of time of N720/A at 1200°C in laboratory air. Creep data from ref [11;29] included.

The effect of intermediate fatigue on creep behavior was less pronounced. Figure 29 shows the creep strain as a function of time at 125 MPa for the two block loading conditions and pure creep loading. Most notably, the material accumulated negligible strain during the 10^5 cycles of fatigue, so that the creep curve produced during the second creep period (labeled A in Figure 29) was a nearly smooth continuation of the first creep curve. The only difference that can be seen is a slight decrease in the creep rate produced during the second creep period. There was no appreciable difference in the creep life.
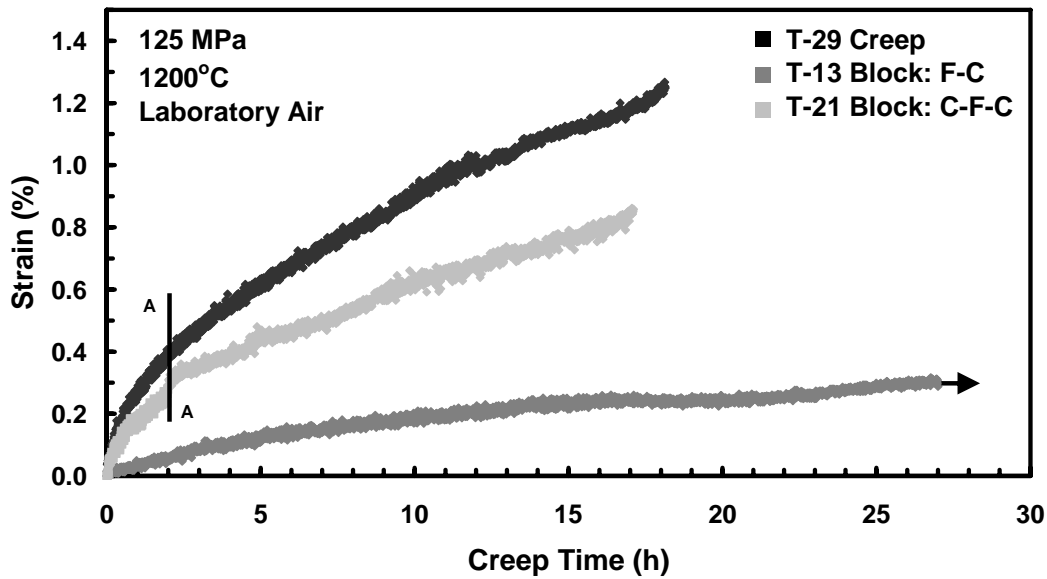
Figure 29. Creep strain as a function of time of N720/A at 125 MPa and 1200°C in laboratory air.

An examination of the creep rate also provides insight into the effects of prior and intermediate fatigue. Creep rate results are shown in Figure 30. At a stress level of 125 MPa, pure creep rates are between 10^{-7} and 10^{-6} s^{-1} and are 10^{-5} s^{-1} at a stress level of 154 MPa. The creep rate of specimens subjected to prior fatigue was 10^{-8} s^{-1} at a stress level of 125 MPa and 10^{-6} s^{-1} at 154 MPa, over an order of magnitude decrease when compared to pure creep. The specimen subjected to intermediate fatigue showed a less pronounced decrease with a creep rate of 10^{-7} after the intermediate fatigue portion of the test.

While intermediate fatigue didn't increase the creep life of the material, it certainly didn't appear to decrease it. It did, however, reduce the amount of creep strain accumulated prior to failure.
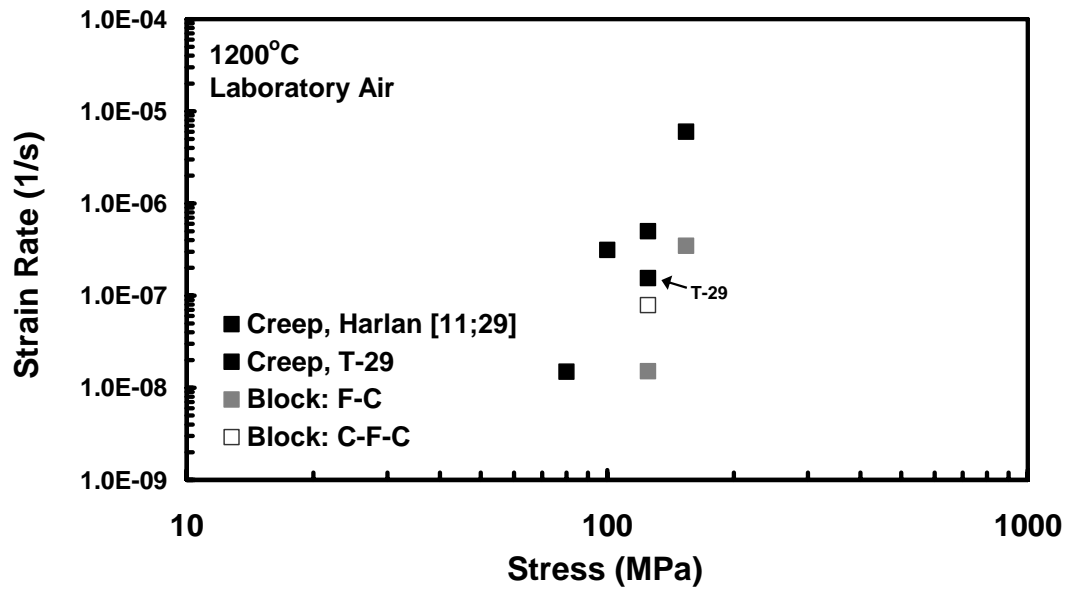
Figure 30. Creep rate vs creep stress for N720/A at 1200°C in laboratory air. Effect of prior fatigue is evident. Pure creep data from Harlan[11;29].

5.2.3 Retained Strength and Stiffness in Laboratory Air

All specimens that achieved a run-out time were subjected to a tensile test to failure at 1200°C to determine the retained strength and modulus. Retained strength and stiffness results are summarized in Table 7. Note that although specimen T-6 achieved a run-out, an error was made in the data collection procedure and no data was recorded.

Table 7. Retained strength and stiffness of N720/A at 1200°C in laboratory air.

Specimen	Prior Loading	Max Stress (MPa)	Test Time (h)	Retained Strength (MPa)	Retained Modulus (GPa)	Strain at Failure (%)
T-6	Cyclic, 10s Hold	100	144	No data	No data	No data
T-10	Cyclic, 100s Hold	125	128	212	50.7	1.14
T-11	Cyclic, 100s Hold	125	113	219	56	1.18
T-13	Block: F-C	125	128	217	59.4	1.04

In all cases, the retained strength was higher than the UTS (186 MPa) of the untested material. Similar results were reported by Eber [10;29] and Steel [34;35] for N720/A specimens subjected to fatigue at 1200°C in laboratory air. Eber suggested that the high strength retention may be a result of the straightening of the fibers during cycling [10:34]. This conjecture could explain the beneficial effects fatigue on subsequent creep performance during the Block: F-C testing. Prior fatigue appears to increase the strength of the material. Therefore, at a given creep stress level, the pre-fatigued material is subjected to creep at a lower percentage of its UTS then the untested CMC. However, when a creep period precedes fatigue cycling (as in Block: C-F-C tests), it appears that enough damage is introduced during the first creep period, that the intermediate fatigue cycling has only a limited effect on subsequent creep behavior.

A negligible difference in retained modulus was measured. The retained modulus was 20% lower than the initial modulus of specimen T-10, was 3% lower for specimen T-11 and 5% higher for specimen T-13. All were within the 48-63 MPa range of initial modulus measured for the specimens. Results are consistent with the damage mechanisms of a fiber-dominated CMC where the stress-strain curve is fairly linear and the material does not appreciably deform plastically.

5.3 Combined Creep-Fatigue Tests in Steam Environment

Eleven combined creep-fatigue tests were conducted at 1200°C in a 100% steam environment. The test results are summarized in Table 8. Note that strain data was not collected for specimens T-7 and T-9 subjected to cyclic loading at a maximum stress

level of 100 MPa with 10 s and 100 s hold times, respectively. These test histories were

repeated using specimens T-24 and T-25. Times to failure produced by specimens T-7/T-

9 were consistent with those produced by specimens T-24/T-25.

Table 8. Summary of N720/A test results at 1200°C in steam environment.

Specimen	Test Type	Max Stress (MPa)	Cycles to Failure	Time to Failure (h)	Strain at Failure (%)
T-7	Cyclic, 10s Hold	100	1516	4.65	No Strain Data
T-24	Cyclic, 10s Hold	100	771	2.36	1.76
T-9	Cyclic, 100s Hold	100	48	1.3	No Strain Data
T-25	Cyclic, 100s Hold	100	40	1.41	1.81
T-15	Block: F-C	100	N/A	27.7 + 0.61	1.65
T-22	Block: C-F-C	100	N/A	1.25	1.35
T-28	Block: C-F-C	100	52620	0.75 + 14.6	1.88
T-16	Cyclic, 10s Hold	125	73	0.23	1.08
T-18	Cyclic, 100s Hold	125	11	0.33	1.26
T-20	Block: F-C	125	83931	23.3	1.77
T-27	Block: F-C	125	67890	18.9	1.94

5.3.1 Cyclic Tests with Hold Times in Steam Environment

Results obtained for N720/A in creep[11;29] and fatigue[10;29] tests conducted at

1200°C in a 100% steam environment are shown in Table 9 in order to facilitate

comparison with results produced in the present effort. As was the case with results

produced in air, the results in steam reveal a much better performance of the material in

fatigue. While run-out was not achieved in the 150 MPa and 170 MPa fatigue tests, the

time to failure in the 150 MPa fatigue tests was two orders of magnitude higher than in

the 154MPa creep test. The creep life at 154 MPa was so short, that creep testing at 170

MPa was not attempted. Also notice that as time to failure decreases, so does strain at failure.

Table 9. Summary of creep[11;29] and fatigue[10;29] test results for N720/A at 1200°C in steam environment.

Data Source	Test Type	Max Stress (MPa)	Cycles to Failure	Time to Failure (h)	Strain at Failure (%)
Harlan [11;29]	Creep	80	N/A	46.1	2.96
Harlan	Creep	100	N/A	2.49	1.41
Harlan	Creep	125	N/A	0.24	0.90
Harlan	Creep	154	N/A	0.027	0.40
Eber [10;29]	Fatigue	100	>100780	>28	Run-out
Eber	Fatigue	125	>166326	>46.2	Run-out
Eber	Fatigue	150	11782	3.27	1.07
Eber	Fatigue	170	202	0.056	0.84

Results of the cyclic tests with hold times are shown in Figure 31 together with creep results from ref [11;29] and fatigue results from ref [10;29]. Unlike in the case of laboratory air, the results obtained in steam were less dramatic. While there was still a large difference between creep and fatigue lives, the lives produced in cyclic tests with hold times were not much different from the creep lives at the same applied stress level. In the case of 100 and 125 MPa tests, the lives obtained in the cyclic tests with hold times were less than an order of magnitude different from creep lives achieved at the same stress level. While times to failure were higher in cyclic with hold times than in pure creep tests at the same stress level, even these differences became less appreciable at higher stress levels. It appears that time at maximum load is critical to material performance in the steam environment. For the cyclic tests with 10 s hold time, time at

maximum load is only 10% less than in a pure creep test. In the case of the cyclic test

with 100 s hold time, time at maximum load is a mere 1% less than that in a pure creep

test. Evidently the loading and unloading between hold times does not allow any

recovery and has no beneficial effect on material durability.
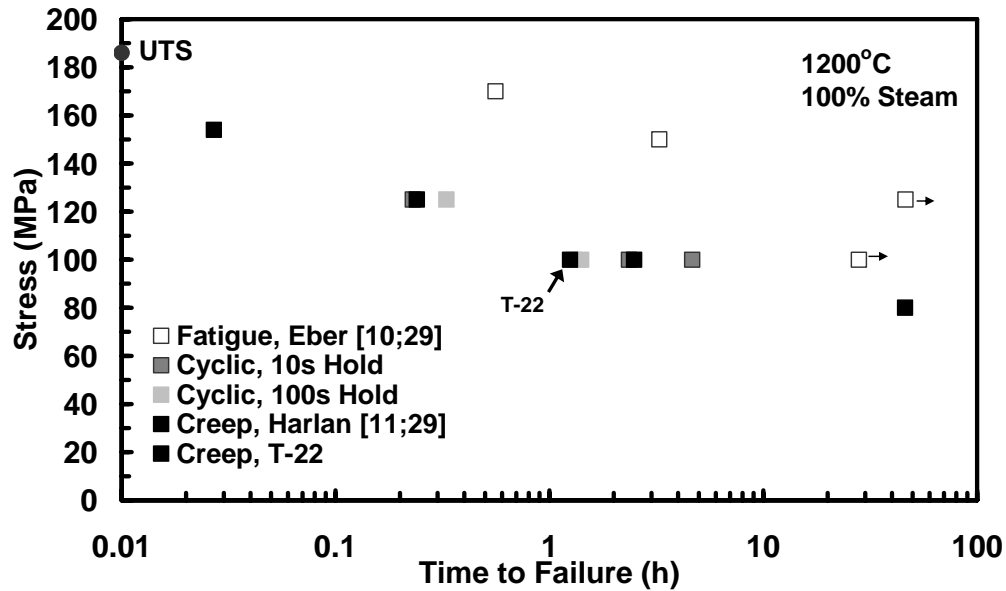
**Figure 31. Maximum stress vs time to failure at 1200°C in steam environment.
Fatigue results from Ref [10;29] and creep results for Ref [11;29] are also included.**

Maximum strains as a function of time for cyclic tests with hold times conducted

at 1200°C in a steam environment are presented in Figure 32 and Figure 33 for maximum

stress levels of 100 and 125 MPa, respectively. Results obtained in creep [11;29] and

fatigue [10;29] tests are also included to facilitate comparison. It is seen that the

evolution of maximum strain observed in cyclic tests with hold times is akin to that

obtained in a creep test conducted at the same applied stress level. In the case of cyclic

test with hold times, maximum strain increases rapidly with time reaching levels close to

those accumulated in creep. Conversely, fatigue tests produced little change in maximum

strain with time. While maximum strain accumulated in cyclic tests with hold time and

in creep tests range from 1.4 to 1.8% at 100 MPa and from 0.75 to 0.95% at 125 MPa,

maximum strain accumulated in fatigue remain below 0.2% for both fatigue stress levels.

These observations once again indicate that the governing damage mechanisms take

place under sustained loading. Furthermore, the presence of steam accelerates damage

growth, thus making even short periods of sustained loading significantly more damaging

than cyclic loading.
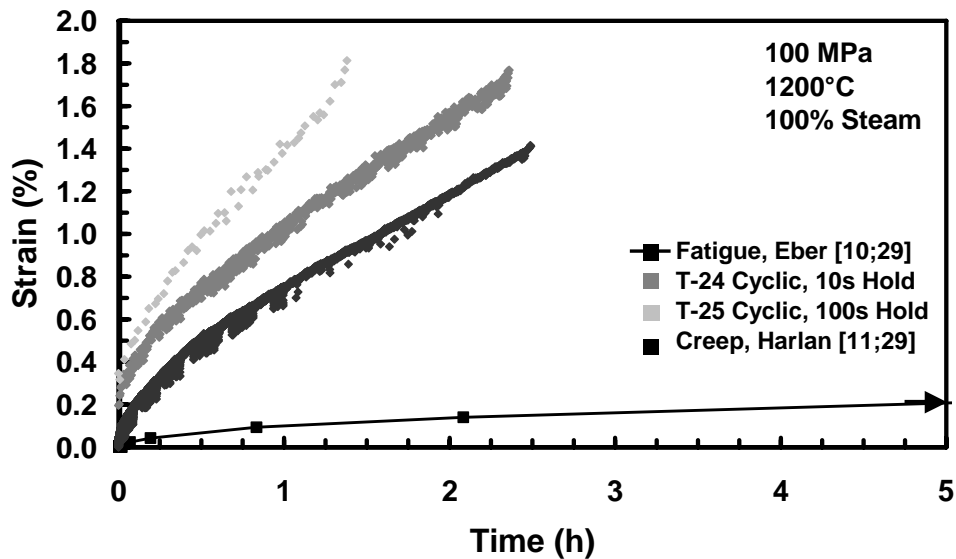
**Figure 32. Maximum strain as a function of time at 1200°C in steam environment
at maximum stress of 100 MPa and. Fatigue results from ref [10;29] and creep
results from ref [11;29] are also included.**
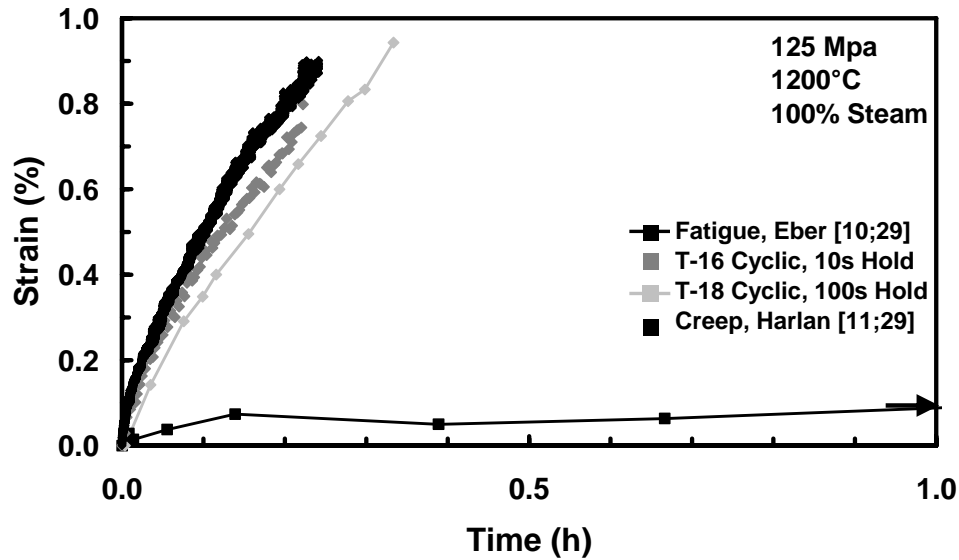
Figure 33. Maximum strain as a function of time at 1200°C in steam environment at maximum stress of 125MPa. Fatigue results from ref [10;29] and creep results from ref [11;29] are also included.

Using the graphs of maximum strain as a function of time, the steady-state strain rate (i.e. the rate of change of maximum strain with time) was calculated for each of the tests represented in Figure 32 and Figure 33. The steady-state strain rate is shown in Figure 34 as a function of maximum applied stress. Creep [11;29] and fatigue results are also shown for comparison. It is seen that the strain rates obtained in cyclic tests with hold times are close to those obtained in creep tests (~10^{-6} s^{-1} at 100 MPa and ~10^{-5} s^{-1} at 125 MPa). Strain rates produced with hold times of any duration are 1 to 2 orders of magnitude higher than those produced in fatigue tests at a given maximum stress. The damaging nature of sustained load is evident.
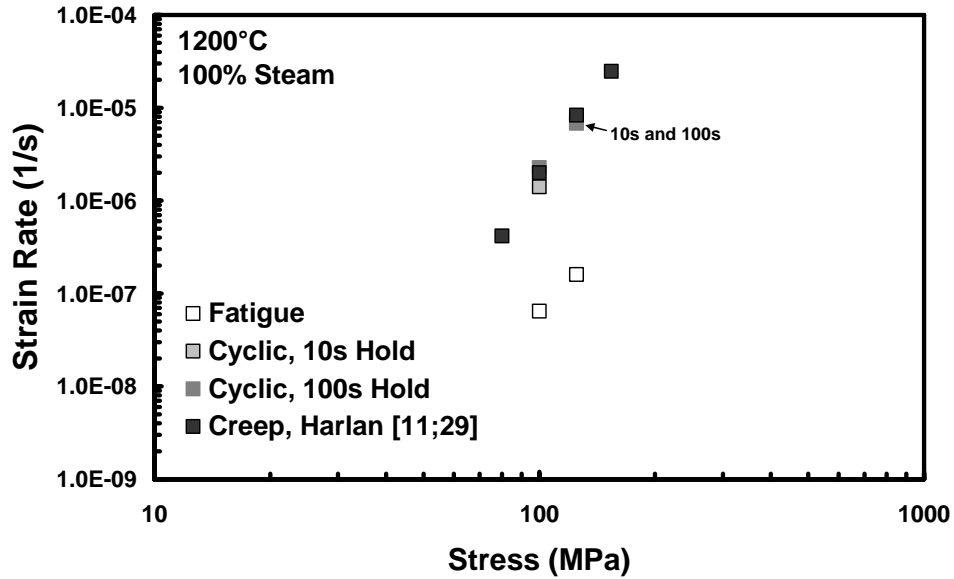
Figure 34. Strain rate as a function of maximum stress at 1200°C in steam environment. Creep data from ref [11;29] are also included.

Figure 35 shows the normalized modulus evolution versus cycles at 1200°C in a steam environment at a maximum stress level of: (a) 100 MPa and (b) 125 MPa. The same characteristics that were observed in air can also be seen in steam. The modulus increases initially and then slowly returns toward the initial modulus. As mentioned previously, modulus increase is a sign of cyclic hardening of the material. All changes in modulus are negligible, even when approaching failure.
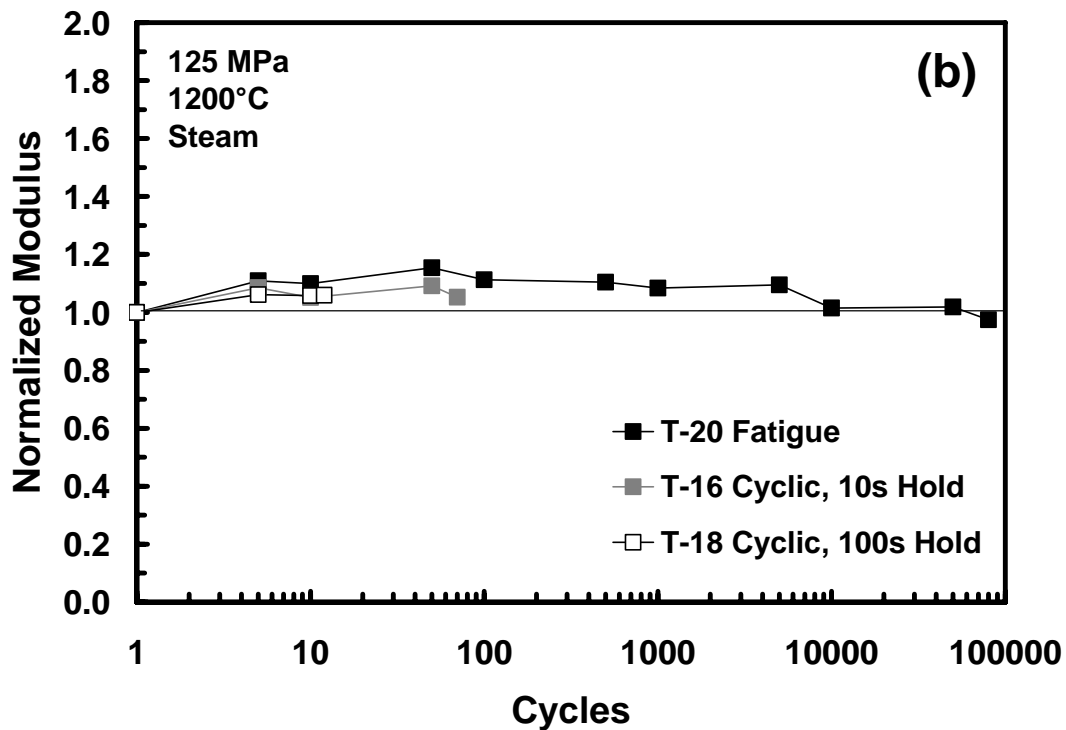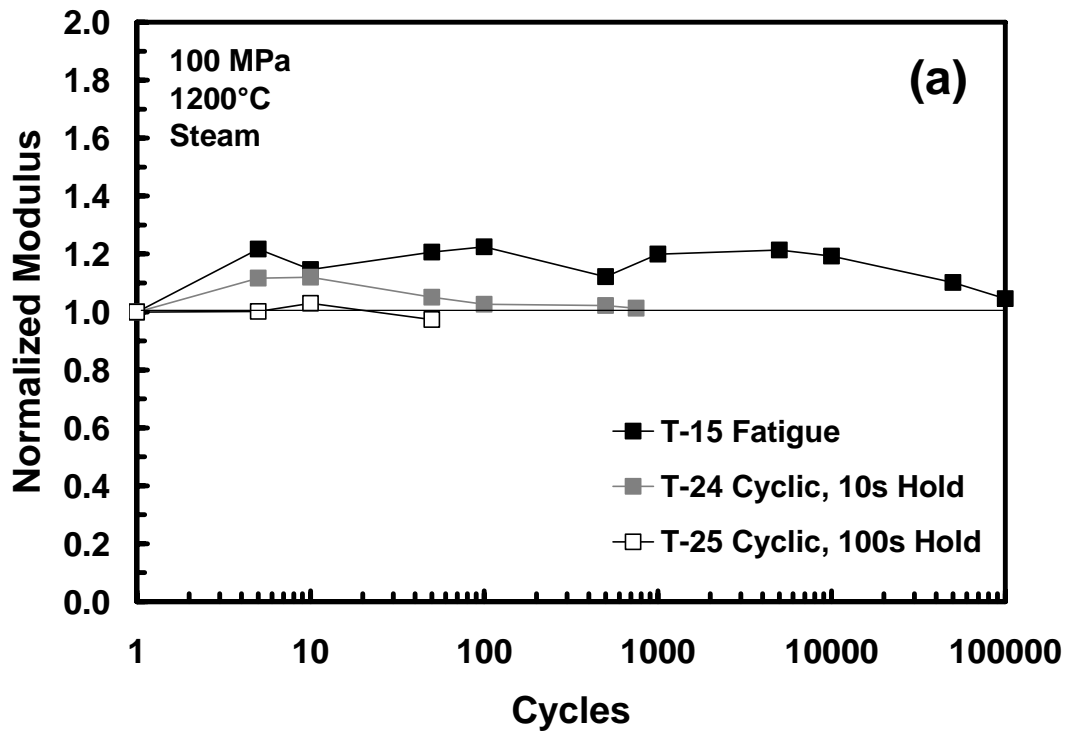
Figure 35. Normalized modulus vs cycles at 1200°C in steam environment for maximum applied stress of (a) 100 MPa and (b) 125 MPa.

5.3.2 Effects of Prior and Intermediate Fatigue on Creep Response in Steam Environment

The effects of prior and intermediate fatigue on the creep behavior of N720/A in a steam environment were also studied. Although Eber [10;29] reported a fatigue run-out (10^5 cycles) at 125 MPa and 1200°C in a steam environment, three specimens subjected to the maximum stress of 125 MPa in this effort did not achieve a run-out. Two specimens (T-20 and T-27) failed after 83931 and 67890 cycles. The third specimen (T-23) survived 75000 cycles, at which point a temperature controller malfunction interrupted the test procedure and the specimen was subjected to an unplanned 6 h at 63 MPa. Fatigue testing of this specimen was not resumed. Maximum strains produced in these tests are shown as a function of time in Figure 36 as well as results reported by Eber [10;29] for comparison.

It is noteworthy that the strain accumulated during fatigue cycling of the three specimens described above are approximately 4 times that reported by Eber [10;29]. Higher accumulated strains are consistent with shorter fatigue lives. The difference between results obtained in this study and the data reported by Eber [10;29] may be due to variation in test specimens, particularly between different panels . The author does not know of any other reason for the discrepancy and is confident in his test procedures and execution. Other researchers have also reported variations in test data. Casas and Martinez-Esnaola reported considerable scatter between two nominally identical tests of an oxide/oxide CMC [6].
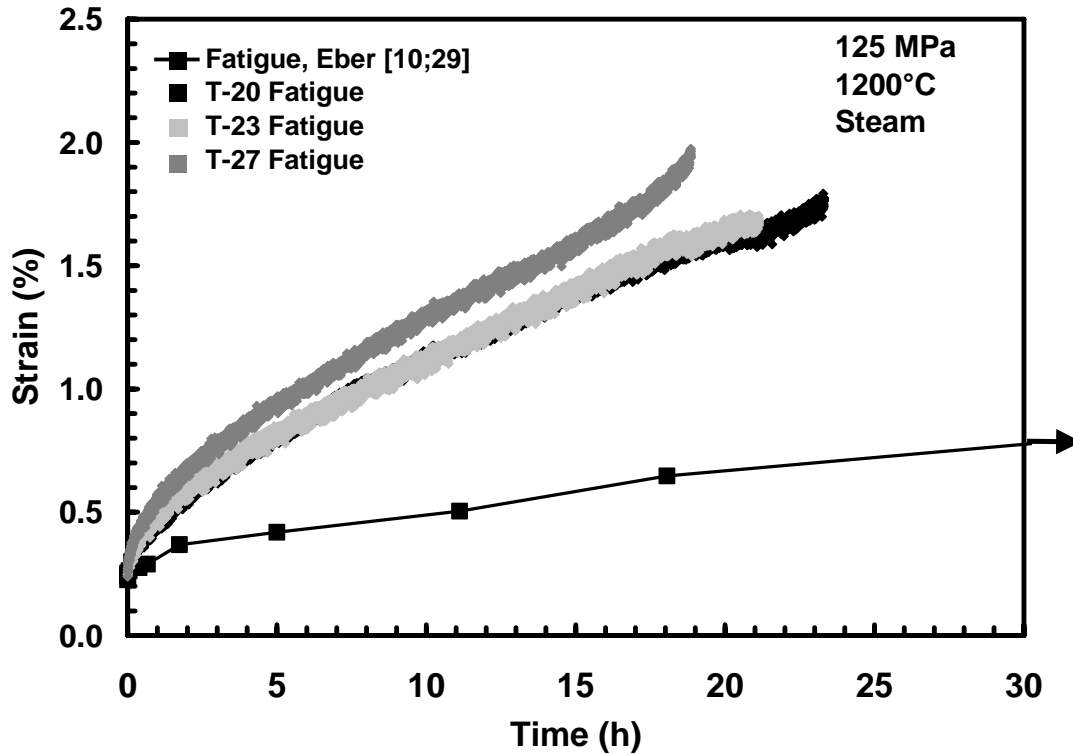
Figure 36. Maximum strain as a function of time at 1200°C in steam environment. Results reported by Eber [10;29] are also included.

Figure 37 shows the results of the prior and intermediate fatigue tests for the 100 MPa stress level. Specimen T-22 was subjected to a Block: C-F-C test at 100 MPa, but an incorrect procedure entry allowed the specimen to creep for longer than the desired 0.75 h, resulting in specimen failure after 1.25 h of creep before any intermediate fatigue cycling commenced. Specimen T-28 was a repeat of the Block: C-F-C test at 100 MPa. It survived the desired 0.75 h of creep prior to intermediate fatigue where it failed after 52620 cycles.
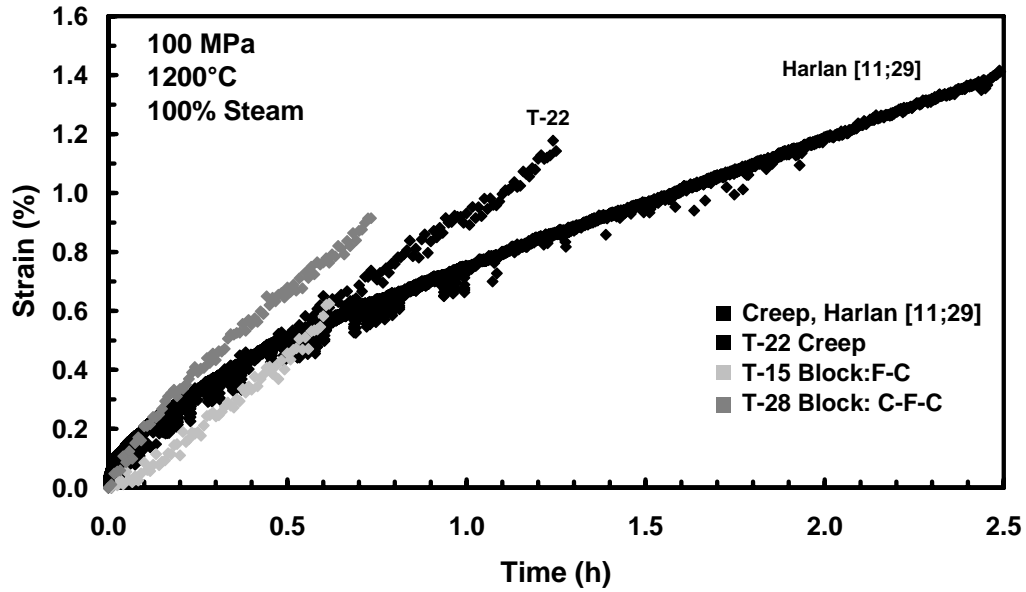
Figure 37. Creep strain vs time at applied stress of 100 MPa at 1200°C in steam environment. Creep data from ref [11;29] also included.

It is seen in Figure 37 that prior fatigue did not have a significant affect on subsequent creep response. Creep strain and time to rupture produced by a prefatigued specimen are within the scatter based on results obtained in creep tests conducted on virgin specimens. The creep strain obtained for virgin specimens was between 1.2% and 1.4% (note that T-28 did not fail at 0.75 h, but continued into an intermediate fatigue portion), with the creep strain produced by a prefatigued specimen falling below this range at 0.7%. The time to rupture for the virgin specimens was between 1.25 and 2.5 h, whereas the time to rupture of the prefatigued specimen was 0.61 h. While the results show that prior fatigue did not improve the creep performance of the material, based on the scatter in the data, more tests would need to be conducted to conclude a detrimental effect on creep performance in a steam environment.

59

It is noteworthy that a higher creep strain and a longer creep life were reported by

Harlan [11;29] for the same test condition. Panel-to-panel and specimen-to-specimen

variations may be the reason for this discrepancy.

The effects of prior creep on the fatigue behavior of the material were

investigated. Specimen T-28 was subjected to 0.75 h of creep test at 100 MPa followed

by fatigue loading with the same maximum stress. Results are presented in Figure 38

where maximum strain (produced in fatigue cycling) is shown as a function of time.
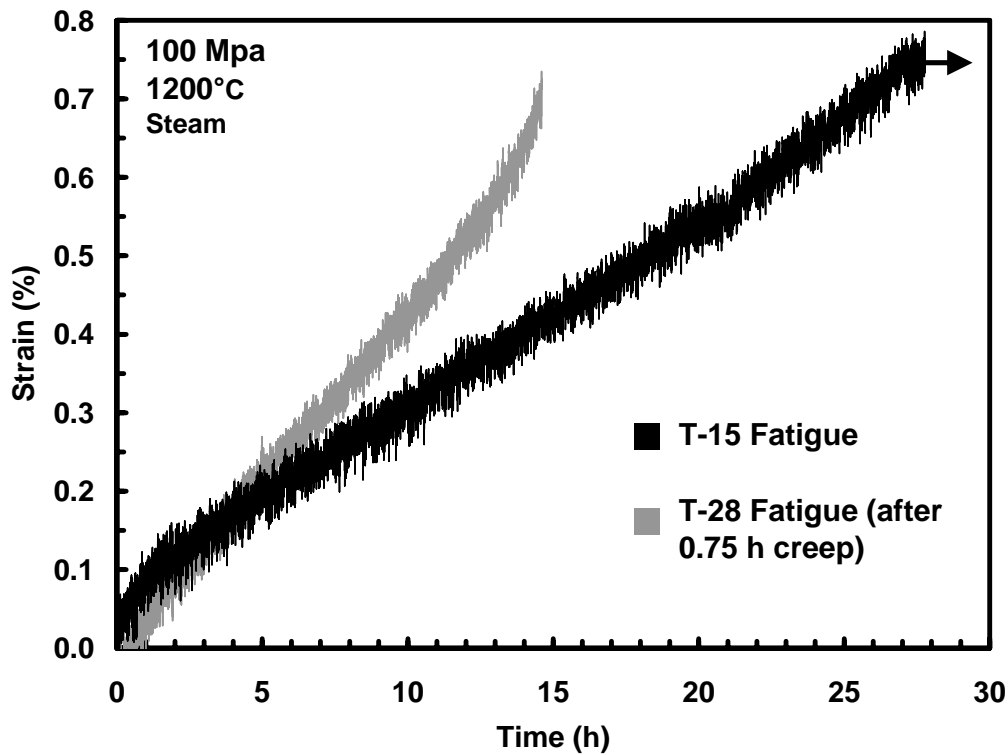
Figure 38. Maximum strain as a function of time for fatigue tests at 1200°C in steam environment.

It can be seen that in steam environment, prior creep significantly reduces the

fatigue life of the material. The specimen subjected to prior creep failed after 52,620

cycles while the specimen subjected to fatigue cycling only achieved a run-out of 10^5 cycles. Obviously, prior creep causes considerable damage to the material. .

5.4 Effect of Steam Environment on Material Response in Combined Creep-Fatigue Tests

Harlan[11;29] and Eber[10;29] both reported a significant reduction in creep and fatigue lives, respectively, due to the presence of steam. The mechanism of this is not yet understood. As discussed before, the impetus for the development of oxide-oxide composites was to chemically stabilize the material for use in oxidizing environments. The considerable difference in results obtained in air and steam environments was somewhat of a surprise.

The difference in material response between the two environments can clearly be seen in Figure 39, where maximum stress is plotted versus time to failure for cyclic tests with hold times performed in this effort. A demarcation line has been drawn to separate results obtained in air from those obtained in steam.

Maximum strain accumulation in cyclic tests with hold times in air and steam environments are plotted as a function of time in Figure 40. Because of the results reported by Harlan [11;29] and Eber [10;29], it had been decided to perform the tests in laboratory air at higher stress levels. The 125 MPa stress level was common to both environments. It is seen in Figure 40 that strain accumulates much more quickly in steam environment than in laboratory air.
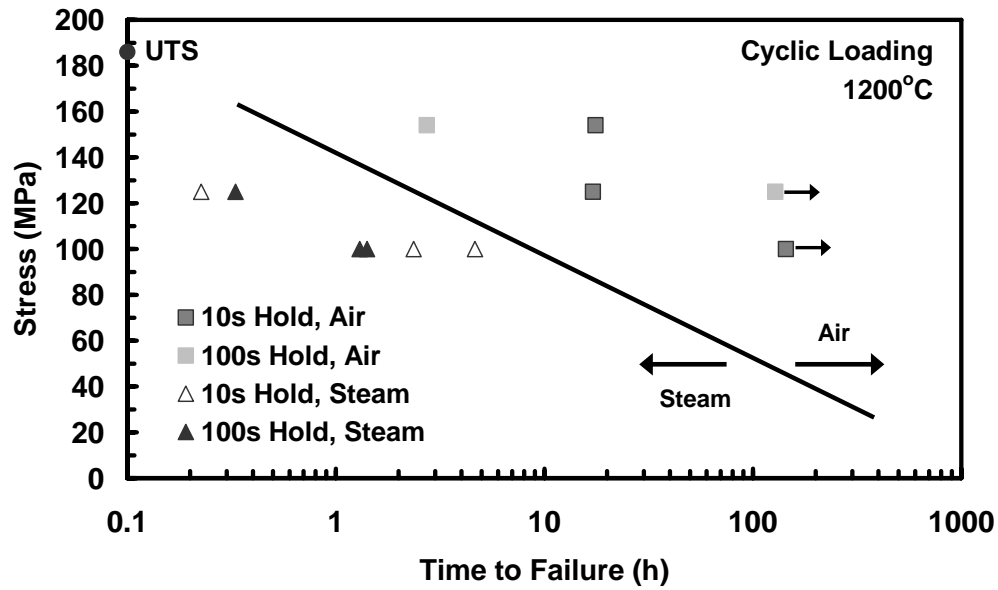
Figure 39. Maximum stress vs time to failure at 1200°C in laboratory air and steam environment.
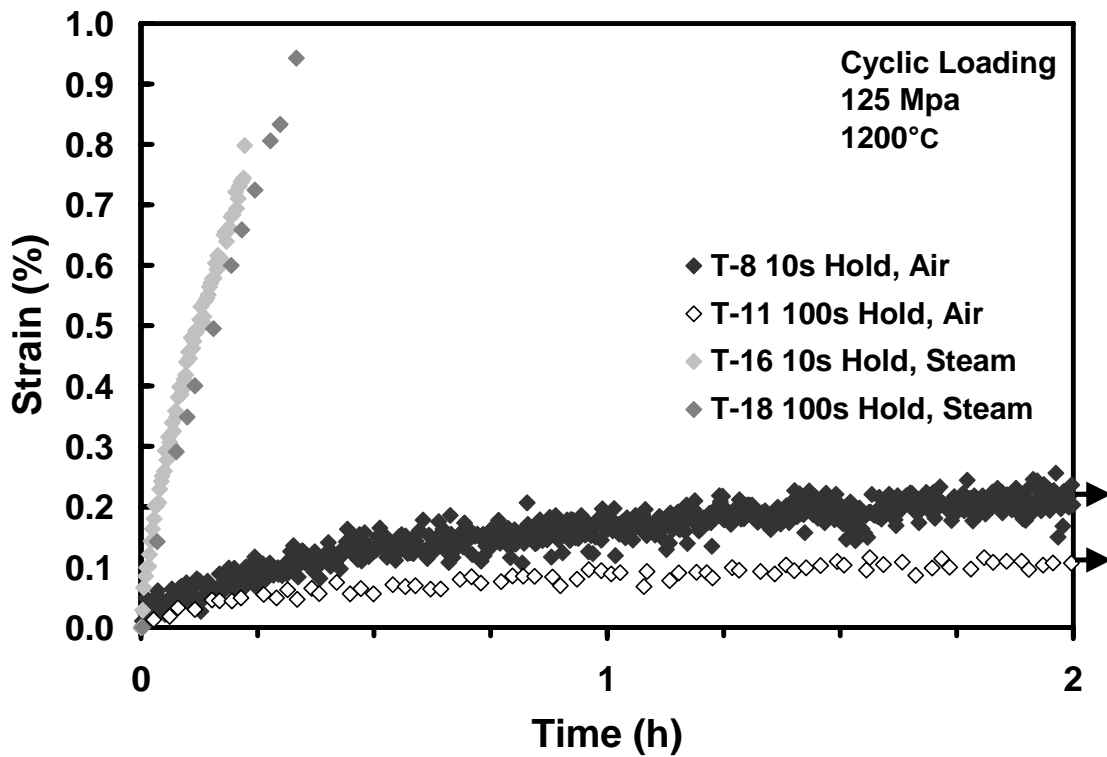
Figure 40. Maximum strain as a function of time for cyclic tests with hold times at 1200°C in laboratory air and steam environments.

Furthermore, when the steady-state strain rate is plotted versus maximum stress, a clear line separates results obtained in steam and laboratory air environments. This can be seen in Figure 41. Steady-state strain rates were two orders of magnitude higher in steam environment than in laboratory air for the same cyclic with hold time test conditions.
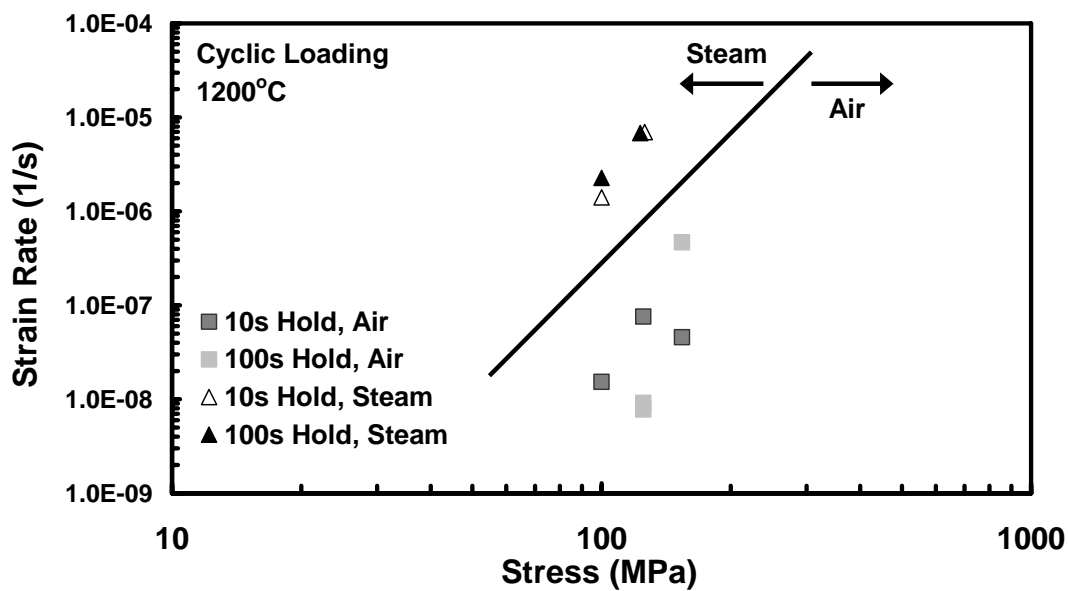
Figure 41. Strain rate vs maximum applied stress for cyclic tests with hold times in laboratory air and steam environments at 1200°C.

5.5 Composite Microstructure

In this section, results from the microscopic characterization of the material will be presented and discussed.

5.5.1 Optical Microscopy

After failure, the specimen fracture surfaces were first observed with an optical microscope. Figure 42 and Figure 43 show the fracture surfaces of the specimens tested under cyclic loading in laboratory air and in steam environments, respectively. Note that T-11, the specimen subjected to cyclic testing with 100 s hold times and maximum stress of 125 MPa in laboratory air, achieved a run-out and failed during the subsequent tensile test. This may have altered the damage mechanisms leading to failure.
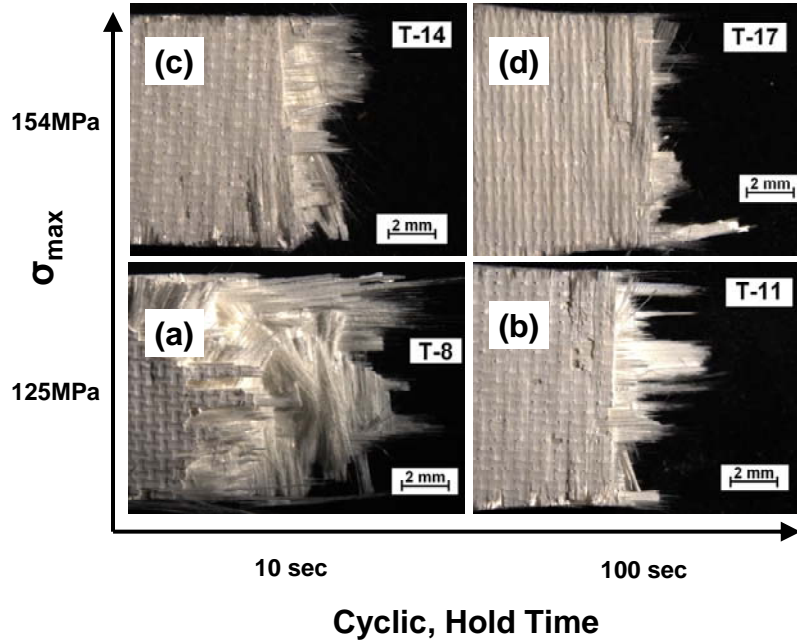
Figure 42. Fracture surfaces of N720/A specimens subjected to cyclic loading with hold times at 1200°C in laboratory air: (a) maximum stress = 125MPa, hold time = 10s; (b) maximum stress = 125MPa, hold time = 100s; (c) maximum stress = 154MPa, hold time =10s; (d) maximum stress = 154MPa, hold time = 100s.
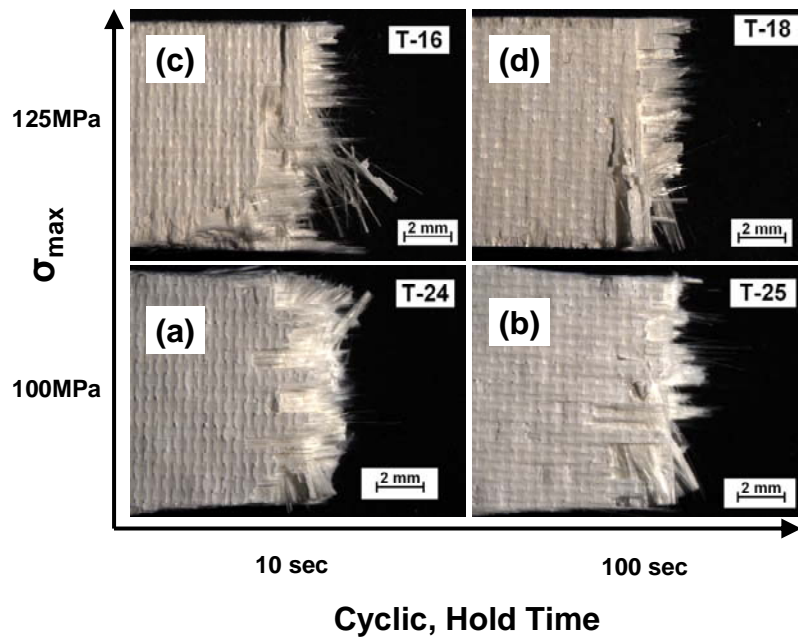
Figure 43. Fracture surfaces of N720/A specimens subjected to cyclic loading with hold times at 1200°C in steam environment: (a) maximum stress = 100MPa, hold time = 10s; (b) maximum stress = 100MPa, hold time = 100s; (c) maximum stress = 125MPa, hold time = 10s; (d) maximum stress = 125MPa, hold time = 100s.

As seen in Figure 42 and Figure 43, the damage zone ranges from ~ 1 to 3 mm in length, except in the case of specimen T-8 subjected to cyclic loading at a maximum stress of 125 MPa and hold times of 10 s where the damage zone approaches ~13 mm in length. There is evidence of both individual fiber pullout and coordinated fracture of fiber bundles. The figures are organized so that the microscopy corresponding to lowest maximum stress and lowest hold time value is in the lower left corner, while the microscopy corresponding to the highest maximum stress level and highest hold time value is in the upper right corner. As evidenced by the data presented in Section 5.2 and 5.3 above, the specimen depicted in the lower left corner has the longest time to failure, and the specimen shown in the upper right corner the shortest time to failure. Individual

fiber pullout generally accompanies delayed failure. This is because the amount of energy dissipated by cracks being deflected around individual fibers is higher than that dissipated when the crack propagates through an entire fiber bundle. The optical micrographs support these observations. Specimens in the lower left corner exhibit more pullout of individual fiber, while those in the upper right corner tend to exhibit a more coordinated fracture as evidenced by the shorter damage zones.
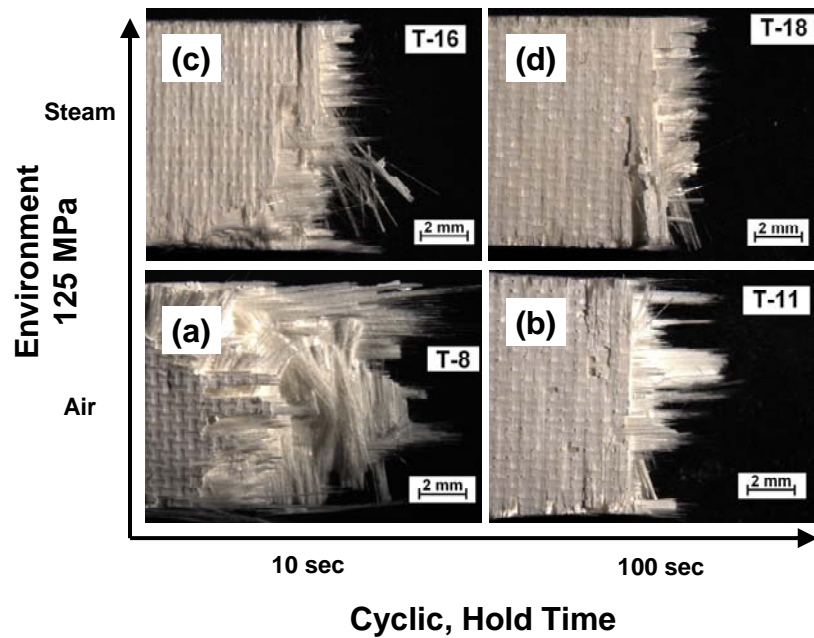
**Figure 44. Fracture surfaces of N720/A specimens subjected to cyclic loading with hold times at 1200°C and maximum stress of 125MPa: (a) air environment, hold time = 10s; (b) air environment, hold time = 100s; (c) steam environment, hold time =10s; (d) steam environment, hold time = 100s**

Figure 44 shows fracture surfaces of specimens tested in laboratory air and in steam environment at a maximum stress level of 125 MPa. The specimens tested in steam had a much shorter time to failure, and subsequently a more planar fracture

surface. This is seen in both the shorter damage zones and less damage to the 90° fiber

bundles.
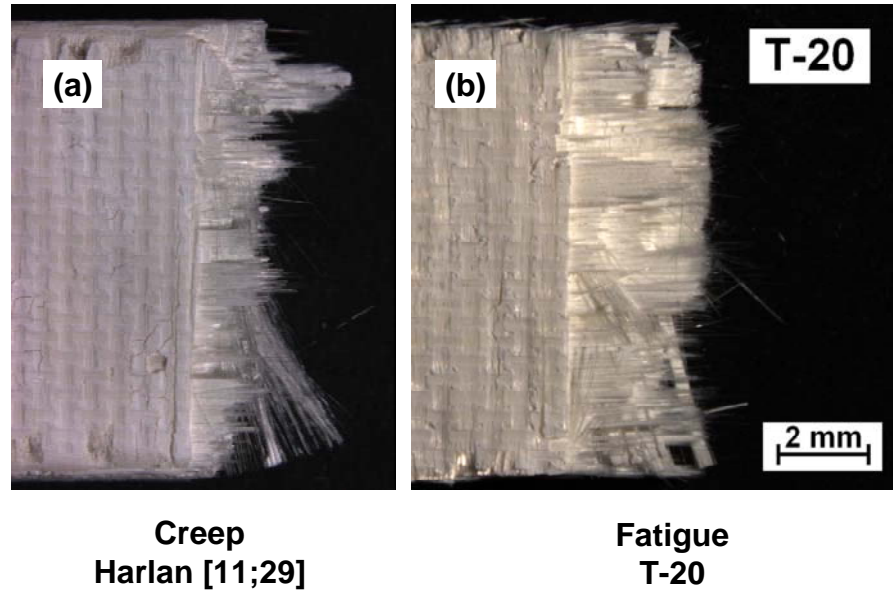
Figure 45. Fracture surfaces of N720/A specimens subjected to testing at maximum stress of 125 MPa and 1200°C in steam environment: (a) creep loading, provided by Harlan [11;29]; (b) fatigue loading.

Figure 45 presents a comparison of fracture surfaces obtained in creep[11;29] and

in fatigue tests conducted with the maximum stress of 125 MPa in steam environment.

Once again, the specimen subjected to fatigue test had a longer time to failure, which

correlates with its longer damage zone and more pullout of individual fibers. Regardless

of loading condition or environment, the fracture surface indicates the time to failure.

5.5.2 Scanning Electron Microscopy

In this section, results of the SEM microscopy characterization will be presented and discussed. First, a general examination of the fiber and matrix is presented. Next, discussion focuses on the typical damage characteristics observed in this study. Lastly, microstructures of the specimens tested under different mechanical loading conditions and microstructures of the specimens tested in different environments are compared and contrasted. An attempt will be made to identify features of the fracture corresponding to a particular loading history and/or environment.

Figure 46 shows SEM micrographs of the N720 fiber (a) and the porous alumina matrix (b) of tested specimens. In Figure 46(a), matrix particles are seen bonded to the fiber. Although N720 fibers have mullite grains ~0.5μm in size, individual grains of the fiber can not be seen. Conversely the grains of the porous matrix with sizes of ~0.5μm and a loose packing are easily distinguishable in Figure 46(b).
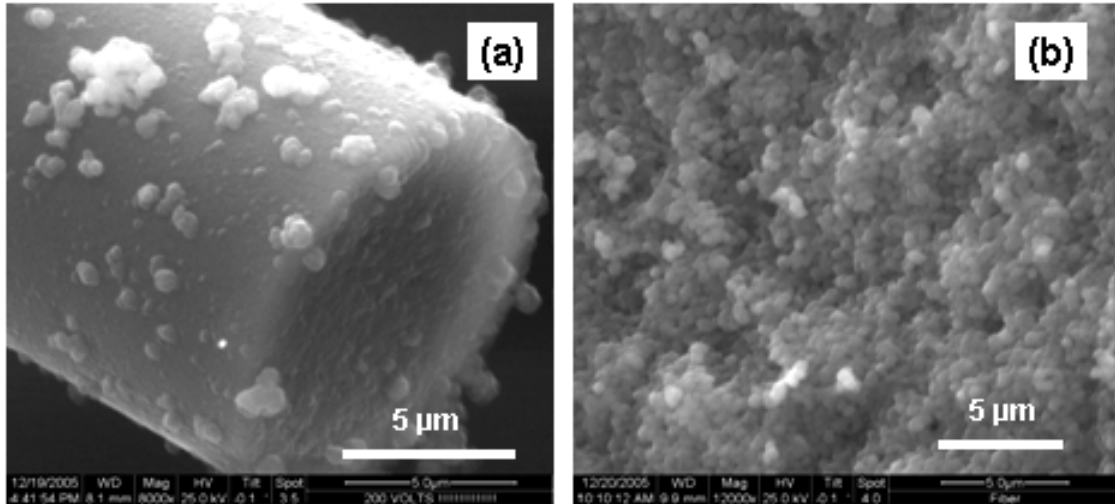
Figure 46. SEM micrographs of: (a) N720 fiber and (b) alumina matrix.
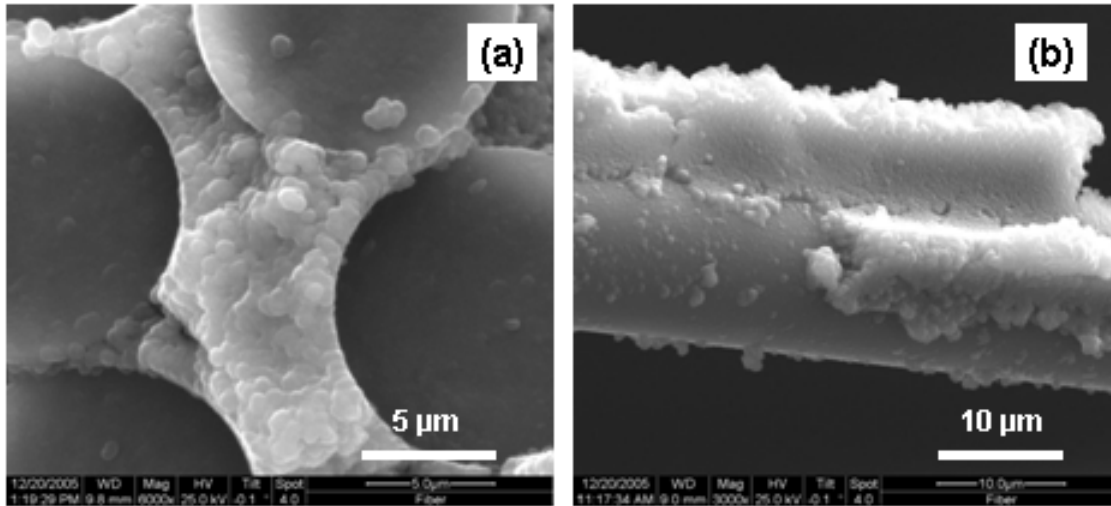
Figure 47. SEM micrographs of N720/A matrix and fiber interface.

Figure 47 shows SEM micrographs of the interface between the fiber and the matrix. The micrograph in Figure 47(a) shows good infiltration of the matrix material in between individual fibers. The micrograph in Figure 47(b) shows the strong bond between the matrix and the fiber. A 90° fiber seen in Figure 47(b) has pulled away from the rest of the bundle, yet matrix material remained bonded to this fiber.

A relatively weak, porous matrix is used in this material in order to allow for crack deflection, i.e. to allow the cracks to propagate around the fibers instead of through the fibers. Figure 48(a) shows crack propagation in the matrix within a 90° fiber bundle, while Figure 48(b) shows a matrix crack propagating around the 0° fibers. It is particularly noteworthy that the crack meanders around the 0° fibers (Figure 48(b)) without causing fiber fracture. The more a crack front is allowed to move through the matrix and deflect around the fibers, the more energy is dissipated leading to longer times to failure.
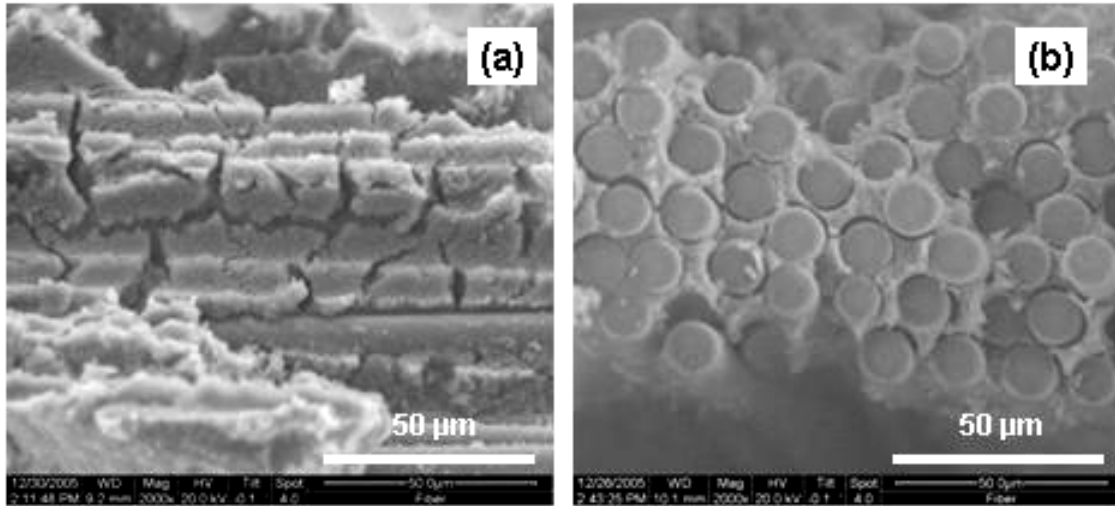
Figure 48. SEM micrographs of matrix cracks in: (a) 90° fiber bundle and (b) 0° fiber bundle. Crack deflection around 0° fibers is evident.
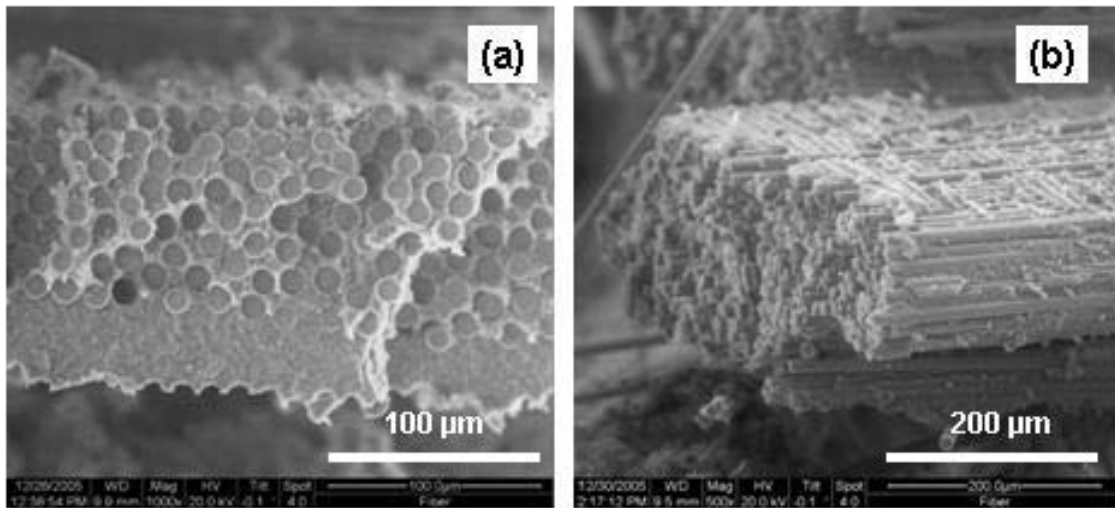
Figure 49. SEM micrographs of planar fracture in tested N720/A material in: (a) 0° fiber bundle and (b) 90° fiber bundle.

Figure 49 shows typical micrographs of coordinated planar fracture of fiber

bundles. The micrograph in Figure 49(a) shows such failure in a 0° bundle while a 90°

bundle failure is shown in Figure 49(b). Planar fracture surface is indicative of a fast failure process where the crack front propagated rapidly through both matrix and fibers. Notice that there are no cracks in the matrix between the fibers, crack deflection did not occur.

In contrast to coordinated planar fracture, individual fiber pullout typically accompanies longer times to failure. Figure 50 shows examples of typical fiber pullout seen for this material. Individual fibers break in different planes where the localized stress increase can be absorbed by adjacent fibers. At first the individual fiber breaks are randomly distributed throughout the bundle. Only after the density of fiber breaks in any particular area reaches a critical value, does the localized stress become high enough to cause bundle failure [9:88-89].
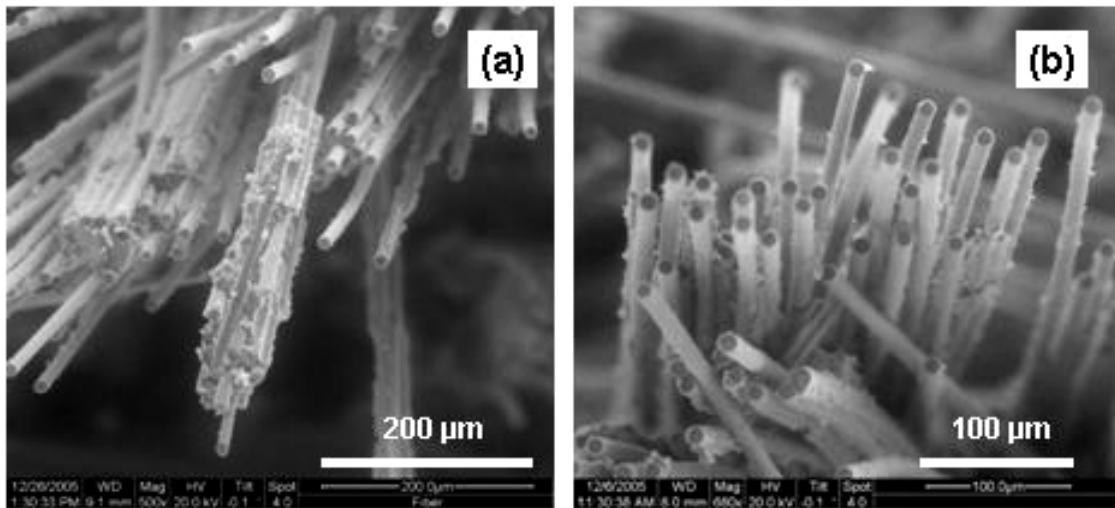
Figure 50. SEM micrographs of fiber pullout in tested N720/A material.

Based on the results of the mechanical tests and the subsequent optical microscope observations, the focus of the SEM investigation was on the amount of coordinated fiber bundle fracture. Individual fiber pullout was more difficult to observe

in the SEM because of the limited focal distance, however, cases of fiber pullout will be presented and discussed.

Maximum stress level, loading history and environment were the three variables in this research. The effect of stress level on the time to failure was readily seen. For a given loading history and environment, time to failure decreased with increasing maximum stress. Testing at the 125 MPa maximum stress level was common to all loading types and environments. Since stress level doesn't change the damage mechanisms, just amplifies them, specimens tested with the same maximum applied stress, but under different loading histories and environments were examined.

First, the effect of environment was considered by examining specimens subjected to cyclic loading with 10 s hold times and a maximum stress of 125 MPa in air and steam environments. Fracture surfaces of the tested specimens are in Figure 51. The most information was gathered at magnifications between 100X and 150X. This allowed viewing of multiple fabric plies and fiber bundles for a more complete characterization of the fracture surface as a whole. The time to failure for the specimen tested in air (T-8) was 17.1 h and for the specimen tested in steam (T-16), the time to failure was 0.23 h. It is clearly seen that the specimen tested in air exhibits more individual fiber pullout. While the fracture surface produced in steam shows some pullout of individual fibers, it is dominated by regions of planar fracture.
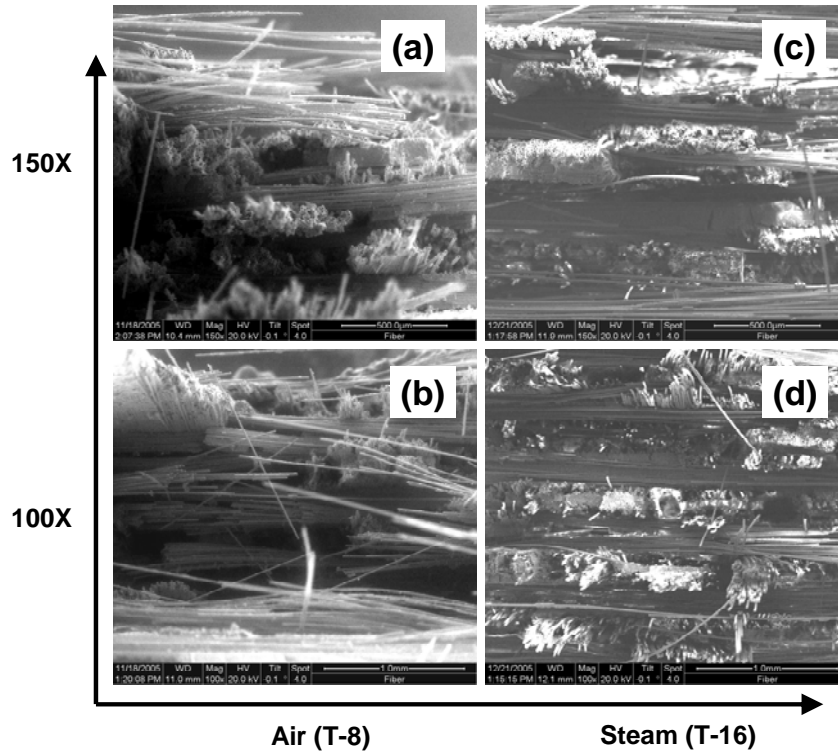
Figure 51. SEM micrographs of N720/A subjected to cyclic loading with 10 s hold time at 125MPa and 1200°C in: (a) air; (b) air; (c) steam; (d) steam.

Next the effect of environment was evaluated by examining specimens tested in creep at 125 MPa in air and steam environments. The resulting micrographs can be found in Figure 52. In the case of steam environment, specimen 13-N tested by Harlan [11;29] was employed. It should be noted that specimen 13-N was coated with gold, which resulted in micrographs with a slightly different appearance. The time to failure for specimen 13-N was 0.24 h while the specimen tested in air (T-29) failed after 23.3 h. While the specimen tested in air does not exhibit as much individual fiber pullout as specimen T-8 discussed above, it still produced a less coordinated fracture surface than the specimen tested in steam. Note that the two comparisons presented here were chosen

because for each pair of specimens, the times to failure differed by approximately two orders of magnitude.
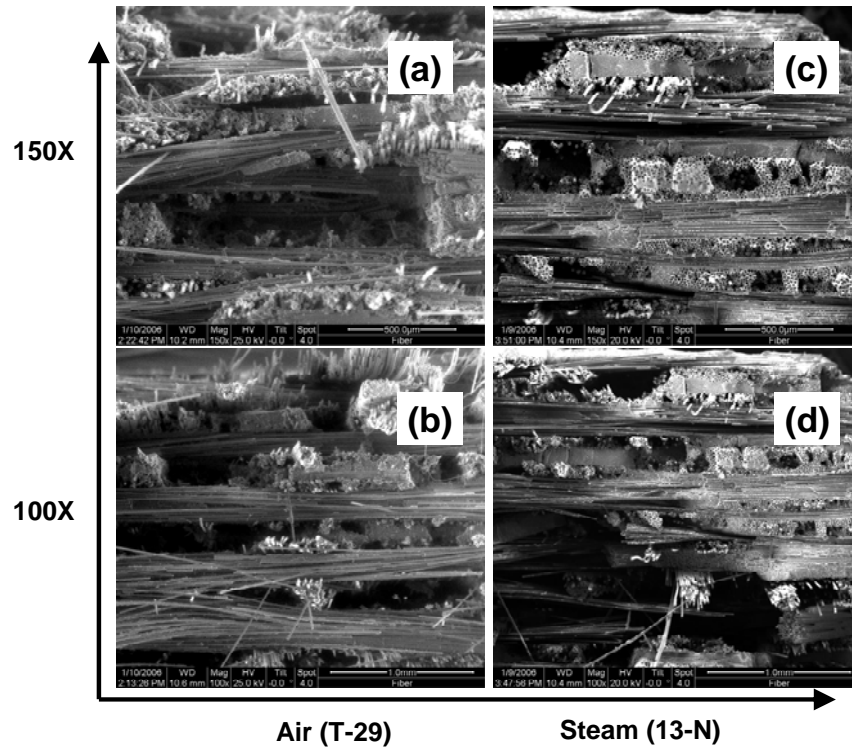
Figure 52. SEM micrographs of N720/A subjected to creep at 125MPa and 1200°C in: (a) air; (b) air; (c) steam; (d) steam.

To assess the influence of loading type on microstructure, specimens tested in creep and fatigue at a given maximum stress level were selected. Because all fatigue tests conducted in air achieved a run-out, a specimen (T-20) tested in steam environment that actually failed in fatigue was chosen. The creep specimen, 13-N, was used for this comparison as well. Specimen T-20 failed in fatigue after 23.3 h. The micrographs are presented in Figure 53. Note that, the creep test, with a shorter time to failure, shows more regions of coordinated fracture. Furthermore, there was less separation of fibers in the 90° fiber bundles. As was the case with the optical micrographs, the SEM

micrographs allow the fracture surfaces corresponding to different failure times to be readily distinguished. However, the fracture surfaces produced in the two environments or under various types of loading are not sufficiently different. The fracture surface topography does not appear to vary significantly with test type or test environment.
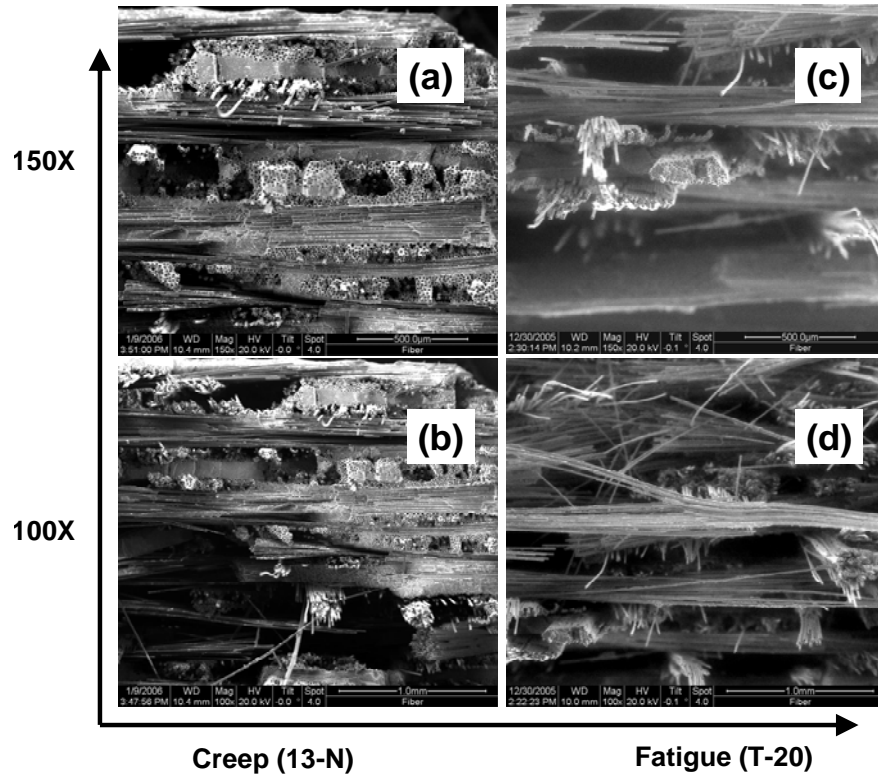
Figure 53. SEM micrographs of N720/A subjected to maximum stress of 125MPa at 1200°C in steam environment under : (a) creep; (b) creep; (c) fatigue; (d) fatigue.

5.6 Energy Dispersive X-ray Spectroscopy (EDS)

The objective of the spectroscopic investigation was to reveal differences between specimens tested in air and in steam environments. Oxide/Oxide composites were first developed for use in oxidizing environments where chemical stability is important. This

is especially important for the N720/A composite. Since it was designed for application in aircraft turbine engines, it must be able to perform when subjected to water vapor and other oxidizing by-products of combustion. Steam represents one such oxidizing environment.

A study by Wannaparhun et al. [38;39] examined N720/A CMC subjected to high temperature and a water-vapor environment and concluded that SiO_2 could be leached out of the mullite phase of the fiber under those conditions. Since the mullite phase was specifically added to the fiber to address the low creep life of a purely alumina fiber, it was suggested that silicon leaching might lead to a reduced creep life of the material in a water-vapor environment.

A qualitative EDS analysis was initiated to determine whether loss of the mullite phase from the fiber could be a reason for the large difference in time to failure observed for specimens tested in the laboratory air and those tested in steam environments. Three specimens were used in this examination: the as-received material, and specimens T-8 and T-16 tested under cyclic loading conditions with a 10 s hold time at 125 MPa, in laboratory air and steam environments, respectively. All specimens were carbon coated for use in the high vacuum mode of the SEM. For the qualitative characterization, it was decided to not polish the fracture surface of the tested specimens. This meant that the results could not be quantified, but would indicate whether SiO_2 leakage has occurred. If it was found to be plausible, then the tested specimens could be polished at a later date, and a more thorough analysis conducted. The as-received material sample was mounted and polished.

Besides the fracture surface, all other variables were controlled as much as possible. Instead of rastering across a surface, the electron beam spot mode was chosen in order to precisely control the beam placement. The working distance to the specimen was set to 10mm, per manufacturer's recommendation. Spot size and electron column voltage were adjusted so that the counts per second were within the recommended range of 1000-2000 and the dead time was between 20-40 %.
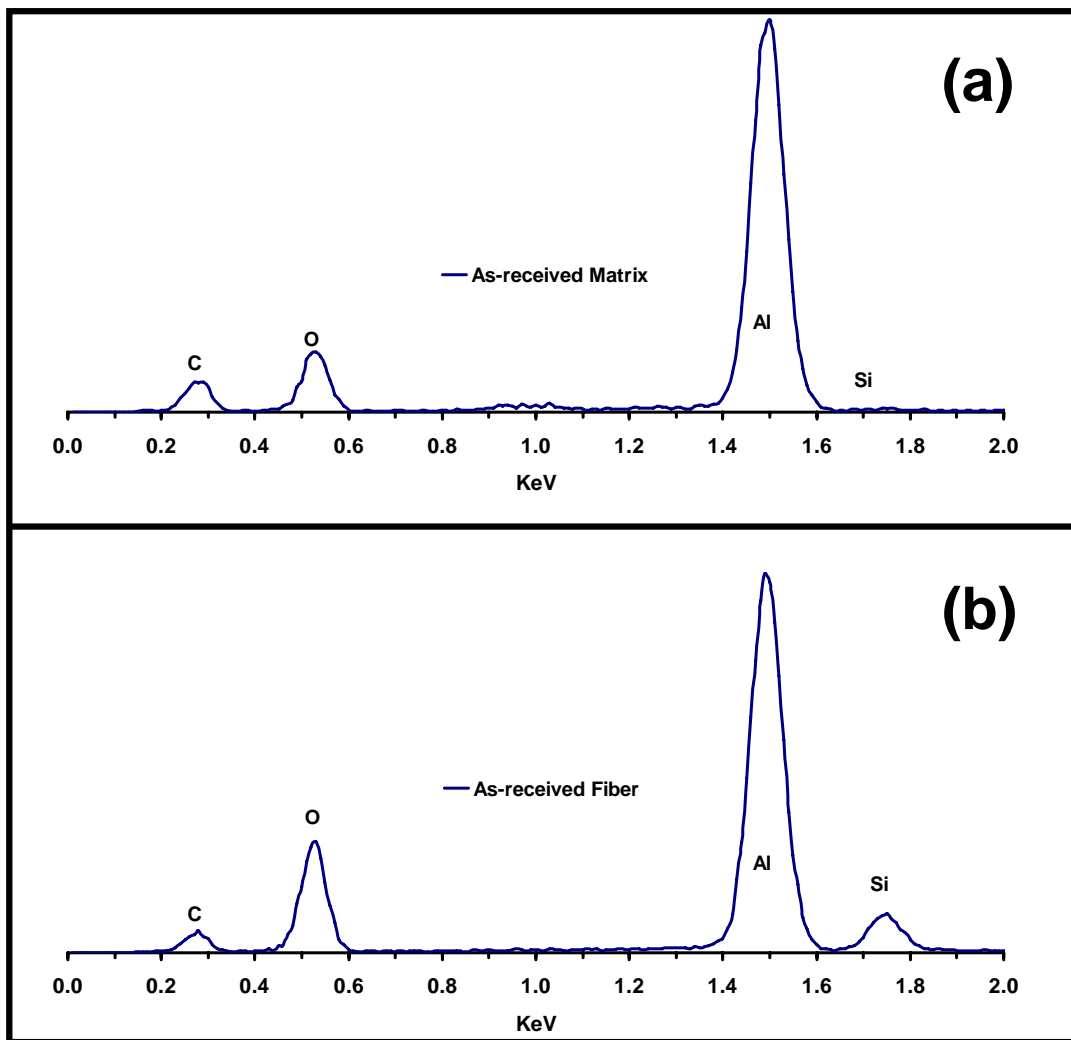
Figure 54. EDS spectra of as-received N720/A composite: (a) matrix and (b) fiber.

Results obtained for the as-received material as shown in Figure 54. As expected, four main peaks were found: carbon (from the coating), aluminum and oxygen (from the alumina and mullite), and silicon (from the mullite). There was also a small peak of copper in the matrix which came from the resin used to mount the specimen for polishing. It is most important to note that silicon was only found in the fiber. Wannaparhum et al. [38;39] found that the silicon was released from the mullite in the form of $Si(OH)_4(g)$ and found evidence that it could recondense within the alumina matrix at the surface. Since it was demonstrated that the as-received matrix showed no silicon peak, it was decided to search for evidence of silicon in the matrix near the edge of fibers.

The electron beam of an SEM has a tear drop shaped reaction volume beneath the surface, from which the secondary electrons are emitted. This limits how closely the electron beam can be focused next to a fiber. Even if the electron beam was focused at the matrix next to a fiber, the reaction volume could include the fiber and thus contaminate the results. To analyze the spectra of the matrix as close to a fiber as possible, regions of the specimens were located where fiber had pulled away from the matrix. This allowed analysis of the matrix that was in direct contact with fiber prior to failure. It also ensured that the reaction volume was not contaminated by any fibers. Figure 55 shows the regions of the two specimens that were analyzed. It also shows where the electron beam was focused for spectra collection (white dots). Two points in the matrix were analyzed: one that was near a fiber edge prior to failure and one that was ~ 25μm away from any fibers.

T-8 Laboratory Air   **T-16 100% Steam**

(a)   (b)

Matrix Near Fiber Edge   **Matrix Away From Fiber**
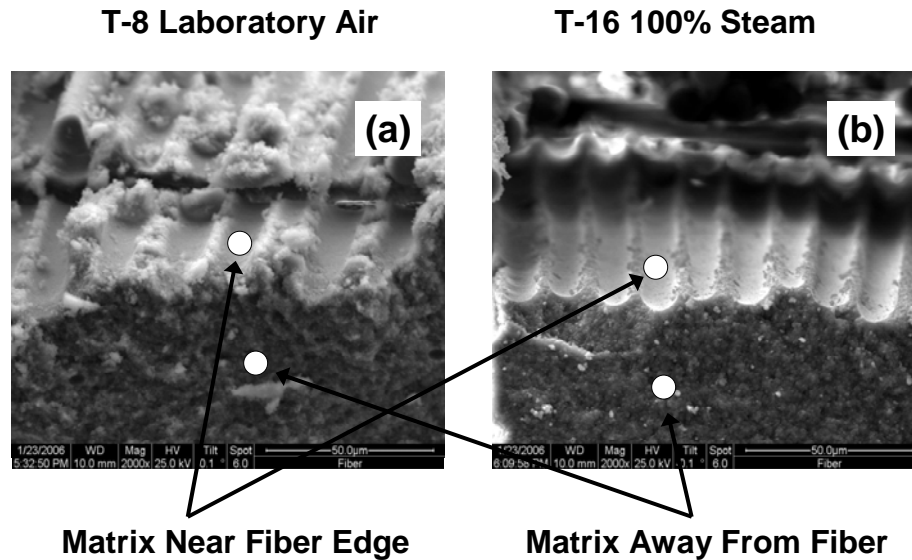
Figure 55. SEM micrographs showing-locations of electron beam for EDS analysis in specimens tested in (a) laboratory air and (b) steam.

Since a direct quantitative analysis could not be accomplished, the results were assessed in three different ways. Figure 56 shows the matrix spectra of the as-received material compared to the matrix spectra obtained near the edge of the fiber for specimens tested in: (a) laboratory air and (b) steam. The matrix spectrum of the specimen tested is laboratory air shows a silicon peak which is slightly greater than that for the as-received material (Figure 56(a)). The matrix spectrum of the specimen tested in steam shows a much more defined silicon peak than the spectrum of the as-received material.
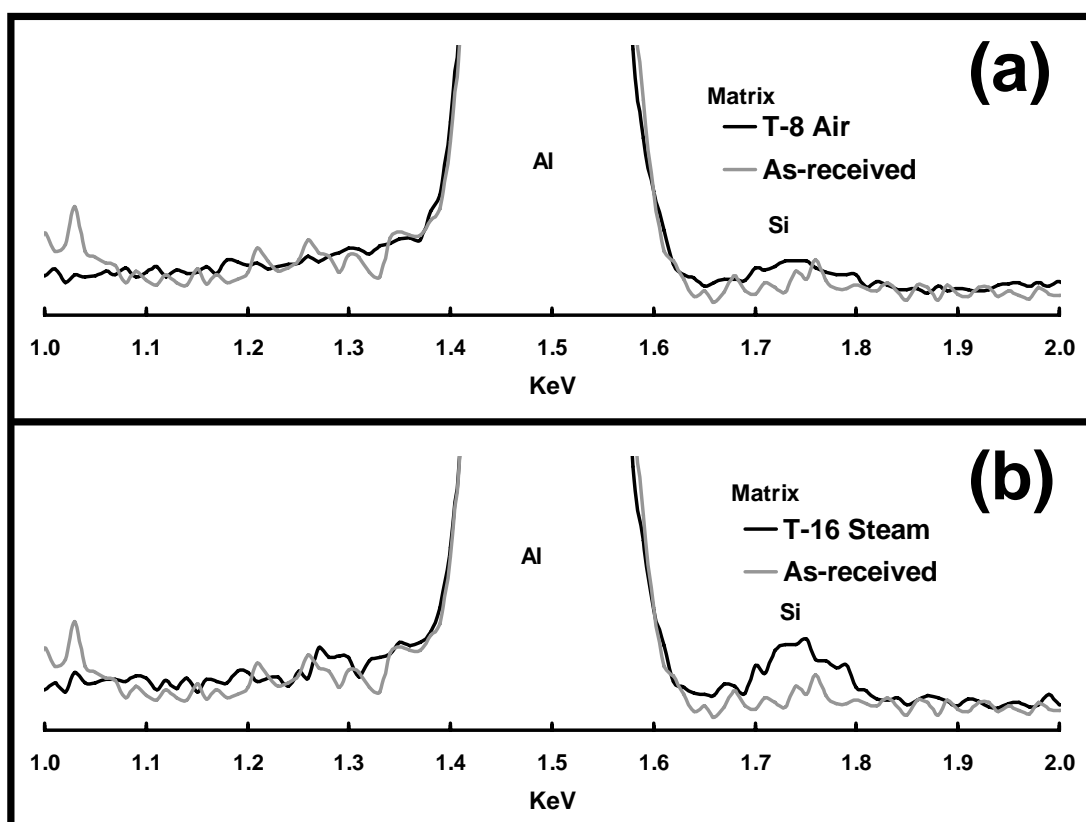
Figure 56. EDS spectra of the matrix of the as-received N720/A CMC compared to the spectra of matrix near the fiber edge of specimens tested in: (a) laboratory air and (b) steam environment.
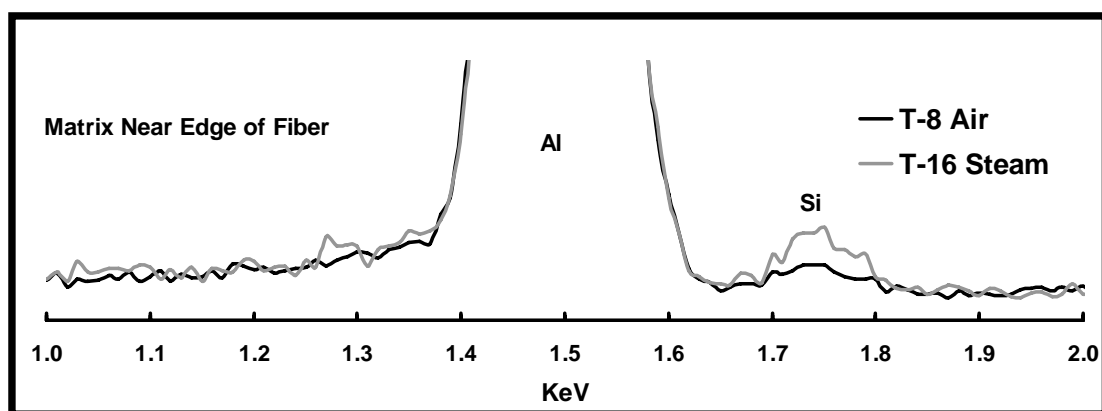
Figure 57. EDS spectrum of the matrix near the fiber edge of N720/A specimens tested in air compared with spectrum of matrix near the fiber edge of specimen tested in steam environment.

The spectra of the matrix at the fiber edge obtained for specimen tested in laboratory air and in steam are compared in Figure 57. Note that the silicon peak is noticeably higher in the case of the specimen tested in steam.
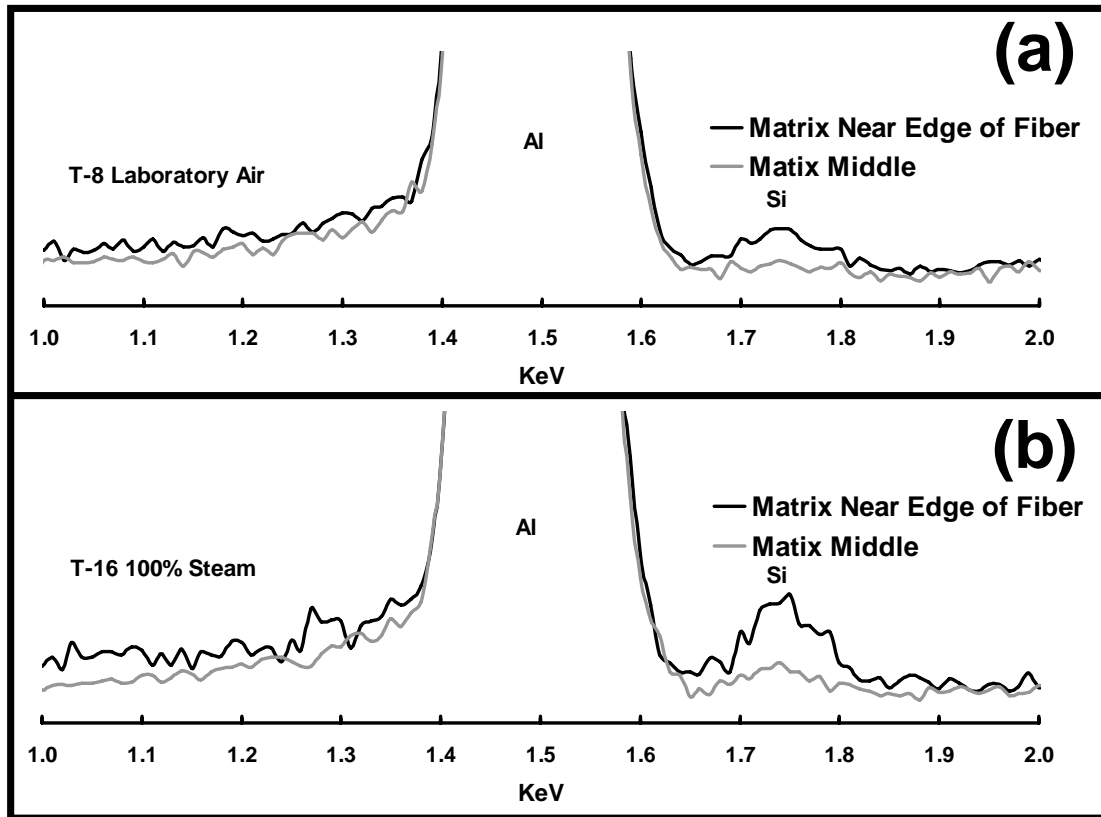
Figure 58. EDS spectra of the matrix near the fiber edge of N720/A CMC compared to the spectra of matrix ~25μm away from fiber edge tested in: (a) laboratory air and (b) steam environment.

Figure 58 shows the spectra of the matrix at the fiber edge compared to the spectra of the matrix located away from the fiber edge for specimens tested in: (a) laboratory air and (b) steam environment. The spectra in Figure 58(a) obtained from the specimen tested in laboratory air show only a slightly higher silicon peak at the fiber

edge. The spectra in Figure 58(b) obtained from the specimen tested in steam show a much larger silicon peak at the fiber edge. In this case, it even appears that the matrix located ~25µm away from the fiber edge shows a small silicon peak.

Results presented in figures X-Y reveal the highest silicon peak at the fiber/matrix interface in the specimen tested in steam compared to silicon peaks for the specimen tested in laboratory air and the as-received material. A smaller silicon peak was found in the specimen tested in laboratory air. This may be a result of the humidity found in the air or water introduced from the waterjet cutting process or cleaning.

VI. Conclusions and Recommendations

6.1 Conclusions

6.1.1 Mechanical Testing in Laboratory Air Environment

Mechanical testing results were consistent with those reported by Harlan[11;29] and Eber [10;29]. At a load rate of 0.0025MPa/s monotonic testing showed negative strain at low stress levels. For specimens tested in laboratory air at maximum stress levels of 125 and 154 MPa, cyclic testing with hold times results were in-between those for pure creep and fatigue alone. Time at maximum stress governs damage accumulation leading to decreased time to failure. Significant modulus changes were not observed during cyclic testing. Prior fatigue improved the creep life of the material by an order of magnitude. Intermediate fatigue had a negligible effect on the creep life.

6.1.2 Mechanical Testing in Steam Environment

In steam environment at stress levels of 100 and 125 MPa, cyclic testing with hold time showed little difference from creep results in time to failure. Time at maximum stress was a greater indicator of time to failure than in the laboratory air environment. Like specimens tested in air, significant modulus changes were not observed during cyclic testing. Prior fatigue reduced the creep life of the material. Specimen did not survive intermediate fatigue. As expected, prior creep reduced the

fatigue life. Results in the steam environment were significantly worse than those in laboratory air. Time to failure and strain rate was reduced by two orders of magnitude.

6.1.3 Composite Microstructure

Optical microscope observations indicated shorter damage zones and a more planar fracture surface as maximum stress level and cyclic hold times increased. The same result was observed as steam was introduced when compared to laboratory air. The damage zone was also smaller in creep loading when compared to fatigue.

SEM micrographs showed a strong fiber/matrix bond as well as crack propagation through the porous matrix. Investigation of fiber bundle failures indicated that as the amount of coordinated fiber bundle failure increased, the time to failure of the specimens decreased. No differences were found in fracture surface microstructure when considering type of loading, stress level or environment when time to failure was the same.

6.1.4 Spectroscopy

Qualitative EDS analysis showed evidence of water vapor attacking the silicon in the mullite phase of the fiber. Silicon peaks were found in regions of matrix bordering fibers in a specimen tested to failure in steam environment. When compared to spectra of as-received material and a specimen tested to failure in laboratory air, the silicon peak was higher in the specimen tested in steam environment. Changes to the mullite phase of the fibers may explain the degraded creep performance of the material in the steam environment.

6.2 Recommendations for Future Research

This research has identified several different paths for continued research. First, a more thorough EDS analysis of polished specimens should be conducted to try and quantify the amount of silicon species leakage comparing as-received, specimens tested in laboratory air, and specimens tested in steam. This would provide a more definitive answer as to whether silicon is migrating from the fibers to the matrix. Ideally, quantitative EDS analysis would be conducted in a Tunneling Electron Microscope (TEM) so effects of the reaction volume of the electron beam would not hinder the quantification of results.

Tunneling Electron Microscope analysis should also be used to identify any grain structure differences between the two tested environments and as-received material. It is the larger, 0.5μm mosaic grains comprised of mullite and alumina that provide the increased creep resistance of the N720 fiber. If a quantitative spectral analysis confirms an increase in silicon in the matrix, it would be beneficial to understand the changes to these grains as the silicon migrates out of the mullite phase of the fiber. A comparison of grain structure could also be used to identify any of the differences seen in the loading conditions.

Changes in the density of the matrix affect the damage tolerance of the material. As density increases, the toughness is reduced. One indication of increased density would be an increased hardness of the matrix. A nanoindentor could be used to measure the hardness of the matrix. Combined with a quantitative EDS analysis as described

above, the hardness could be measured and correlated to the amount of silicon present in the matrix.

Combining the results of the three additional microstructural tests above, might indicate the damage mechanisms responsible for the decreased strength in environment. It could be that the larger grains in the fiber are being changed, reducing the creep resistance of the fiber. Another possibility is that the silicon species migration is changing the characteristics of the matrix, and the propagation of cracks within it. A combination of these two possibilities might also be an explanation.

It may be warranted at this point to consider an interphase coating for use in the N720/A material. Saruhun et al. have demonstrated a process for coating N720 fibers in fabric form with (carbon + ZrO_2) and (carbon + Al_2O_3) using a CVD process. A simple three-point bending test was conducted and the composites were characterized microstructurally with a SEM. They inferred from those results that a fugitive/oxide double layer system showed potential of improving crack deflection and fiber sliding [31]. How this would hold up to a water vapor environment is not known.

Adding an interphase coating to this material would increase the cost to manufacture of the material, negating some of the advantages that oxide/oxide porous matrix composites have over other CMCs. Continued research is however warranted, as adding successful coatings to these materials may give greater insight into their properties and identify other means towards controlling the damage mechanisms.

Bibliography

1. "3M™ Nextel™ Ceramic Fiber Typical Properties" in *3M Nextel™ Ceramic Textiles Technical Notebook*. St. Paul, MN: 3M Corporation, no date.

2. "All you wanted to know about ELECTRON MICROSCOPY but didn't dare to ask!" FEI Company brochure (2004), http://www.feicompany.com.

3. "Report of the Committee on the Definition of the Term Ceramics," *Journal of the American Ceramic Society*, 3(7):526-542 (1920).

4. Baker, A., Dutton, S., Kelly, D. *Composite Materials for Aircraft Structures*. Second Edition. Virginia: AIAA, 2004.

5. The Boeing Company, (Feb 2006), http://www.boeing.com.

6. Casas, L., Martinez-Esnaola, J.M. "Microstructural characterization on an alumina/mullite composite tested in creep," *Materials Science and Engineering*, A368:139-144 (2004).

7. Chawla, K. K. *Ceramic Matrix Composites*. London: Chapman and Hall, 1993.

8. COI Ceramics, Unpublished Data.

9. Daniel, I.M., Ishai, O., *Engineering Mechanics of Composite Materials*. New York: Oxford University Press, 1994.

10. Eber, Chalene A. *Effect of Temperature and Steam Environment on Fatigue Behavior of an Oxide-Oxide Continuous Fiber Ceramic Composite.* MS thesis, AFIT/GA/ENY/05-M09. School of Engineering and Management, Air Force Institute of Technology (AU), Wright-Patterson AFB, OH March 2005.

11. Harlan, Lee B. *Creep-Rupture Behavior of an Oxide/Oxide Ceramic Matrix Composite at Elevated Temperatures in Air and Steam Environments.* MS thesis, AFIT/GA/ENY/05-M05. School of Engineering and Management, Air Force Institute of Technology (AU), Wright-Patterson AFB, OH, March 2005.

12. Haslam, J.J., Berroth, K.E., Lange, F.F. "Processing and Properties of an all-oxide composite with a porous matrix," *Journal of the European Ceramic Society*, 20:607-618 (2000).

13. Haynes, J.A., Lance, M.J., Cooley, K.M., Ferber, M.K., Lowden, R.A., Stinton, D.P. "CVD Mullite Coating in High-Temperature, High-Pressure Air-H_2O," *Journal of the American Ceramic Society*, 83[3]:657-659 (2000).

14. "Turbine Engine Technology, a Century of Powered Flight," program brochure, Air Force Research Laboratory, Wright-Patterson AFB, OH. Gahn, S.M. and Morris, R.W. Eds, n. pag., http://www.pr.afrl.af.mil/divisions/prt.

15. Jacobson, N.S. "Corrosion of Silicon-Based Ceramics in Combustion Environments," *Journal of the American Ceramic Society*, 76[1]:3-28 (1993).

16. Jacobson, N.S., Morscher, G.N., Bryant, D.R., Tressler, R.E. "High-Temperature Oxidation of Boron Nitride: II, Boron Nitride Layers in Composites," *Journal of the American Ceramic Society*, 82[6]:1473-1482 (1999).

17. Jurf, R.A., Butner, S.C. "Advances in Oxide-Oxide CMC," *Proceedings of the 44th ASME Gas Turbine and Aeroengine Congress and Exhibition*, Indianapolis, Indiana, June 7-10, 1999.

18. Kerans, R.J., Parthasarathy, T.A. "Crack deflection in ceramic composites and fiber coating design criteria," *Composites: Part A*, 30:521-524 (1999).

19. Lange, F.F., Tu, W.C., Evans, A.G. "Processing of damage-tolerant, oxidation-resistant ceramic matrix composites by a precursor infiltration and pyrolysis method," *Materials Science and Engineering*, A195:145-150 (1995).

20. LaRochelle, K.J. *Tensile Stress Rupture Behavior of a Woven Ceramic Matrix Composite in Humid Environments at Intermediate Temperatures.* Ph.D. dissertation, AFIT/DS/ENY/05-01. School of Engineering and Management, Air Force Institute of Technology (AU), Wright-Patterson AFB, OH March 2005.

21. Levi, C.G., Yang, J.Y., Dalgleish, B.J., Zok, F.W., Evans, A.G. "Processing and Performance of an All-Oxide Ceramic Composite," *Journal of American Ceramic Society*, 81(8):2077-2086 (1998).

22. Mattoni, M.A., Yang, J.Y., Levi, C.G., Zok, F.W., Zawada, L.P. "Effects of Combustor Rig Exposure on a Porous-Matrix Oxide Composite," *International Journal of Applied Ceramic Technology*, 2(2):133-140 (2005).

23. Milz, C., Goering, J., Schneider, H. "Mechanical and Microstructural Properties of Nextel™ 720 Relating to Its Suitability for High Temperature Applications in CMCs," *Ceramic Engineering and Science Proceedings*, 21[9-10]:191-198 (1999).

24. Morscher, G.N., Bryant, D.R., Tressler, R.E. "Environmental Durability of BN-Based (For SiC/SiC Composites) in H_2O-Containing Atmospheres at Intermediate Temperatures," *Ceramic Engineering and Science Proceedings*, 18[3]:525-533 (1997).

25. Ogbuji, L.U. "Degradation of SiC/BN/SiC Composite in the Burner Rig," *Ceramic Engineering and Science Proceedings*, 19[4]:257-264 (1998).

26. Ohnabe, H., Masaki, S., Onozuka, M., Miyahara, K., Sasa, T. "Potential application of ceramic matrix composites to aero-engine components," *Composites: Part A*, 30:489-496 (1999).

27. Parlier, M., Ritti, M.H. "State of the art and perspectives for oxide/oxide composites," *Aerospace Science and Technology*, 7:211-221 (2003).

28. Parthasarathy, T.A., Zawada, L.P., John, R., Cinibulk, M.K., Zelina, J. "Evaluation of Oxide-Oxide Composites in a Novel Combustor Wall Application," *International Journal of Applied Ceramic Technology*, 2(2):122-132 (2005).

29. Ruggles-Wrenn, M.B., Mall, S., Eber, C.A., and Harlan, L.B. "Effects of Steam Environment on High-Temperature Mechanical Behavior of Nextel™720/Alumina (N720/A) Continuous Fiber Ceramic Composite**,** *Composites: Part A*, in press (2006).

30. Ruggles-Wrenn, M.B., private communications (2005).

31. Saruhan, B., Schmucker, M., Bartsch, M., Schneider, H., Nubian, K., Wahl, G. "Effect of interphase characteristics on long-term durability of oxide-based fibre-reinforced composites," *Composites: Part A*, 32:1095-1103 (2001).

32. Schmidt, S., Beyer, S., Knabe, H., Immich, H., Meistring, R., Gessler, A. "Advanced ceramic matrix composite materials for current and future propulsion technology applications," *Acta Astronautica*, 55:409-420 (2004).

33. Simon, R.A. "Progress in Processing and Performance of Porous-Matrix Oxide/Oxide Composites," *International Journal of Applied Ceramic Technology*, 2(2):141-149 (2005).

34. Steel, Steven G. *Monotonic and Fatigue Loading Behavior of an Oxide/Oxide Ceramic Matrix Composite.* MS thesis, AFIT/GMS/ENY/00M-02. School of Engineering and Management, Air Force Institute of Technology (AU), Wright-Patterson AFB OH, March 2000.

35.   Steel, S.G., Zawada, L.P., Mall, S. "Fatigue Behavior of a Nextel™ 720/Alumina (N720/A) Composite at Room and Elevated Temperature," *Ceramic Engineering and Science Proceedings*, 22[3]:695-702 (2001).

36.   Tressler, R.E. "Recent developments in fibers and interphases for high temperature ceramic matrix composites," *Composites: Part A*, 30:429-437 (1999).

37.   Tu, W.C., Lange, F.F., Evans, A.G. "Concept for a Damage-Tolerant Ceramic Composite with Strong Interfaces," *Journal of the American Ceramic Society*, 79[2]:417-424 (1996).

38.   Wannaparhum, S., Seal, S., Desai, V. "Surface chemistry of Nextel-720, alumina and Nextel-720/alumina ceramic matrix composite (CMC) using XPS-A tool for nano-spectroscopy," *Applied Surface Science*, 185:183-196 (2002).

39.   Wannaparhum, S., Seal, S., Desai, V.H., Varghese, P., Campbell, C.X. "Combined Spectroscopic and Thermodynamic Investigation of Nextel-720/Alumina Ceramic Matrix Composite in Air and Water Vapor at 1100°C", *Journal of the American Ceramic Society*, 86(9):1628-30 (2003).

40.   Wilson, D.M., Lieder, S.L., Lueneburg, D.C, "Microstructure and High Temperature Properties of Nextel 720 Fibers", *Ceramic Engineering and Science Proceedings*, 16(5):1005-1014 (1995).

41.   Wilson, D.M., Visser, L.R. "High performance oxide fibers for metal and ceramic composites," *Composites: Part A*, 32:1143-1153 (2001).

42.   Zawada, L.P. and Lee, S.S. "The Effect of Hold Times on the Fatigue Behavior of an Oxide/Oxide Ceramic Matrix Composite," *Thermal and Mechanical Test Methods and Behavior of Continuous-Fiber Ceramic Composites, ASTM STP 1309*, Michael G. Jenkins, Stephan T. Gonczy, Edgar Lara-Curzio, Noel E. Ashbaugh, and Larry P. Zawada, Eds., American Society for Testing and Materials (1997).

43.   Zawada, L.P. and Staehler, J., Steel, S.G. "Consequence of Intermittent Exposure to Moisture and Salt Fog on the High-Temperature Fatigue Durability of Several Ceramic-Matrix Composites," *Journal of the American Ceramic Society*, 86[8]:1282-1291 (2003).

44.   Zok, F.W., Levi, C.G. "Mechanical Properties of Porous-Matrix Ceramic Composites," *Advanced Engineering Materials*, 3(1-2):15-23 (2001).

Vita

Captain John M. Mehrman graduated from Keene Central High School in Keene, New York. He entered undergraduate studies at Rensselaer Polytechnic Institute in Troy, New York where he graduated with a Bachelor of Science degree in Mechanical Engineering in May 1999. He was commissioned through the Detachment 550 AFROTC at Rensselaer Polytechnic Institute.

His first assignment was at Eglin AFB, Florida as an Advanced Missile Design Engineer for the Air Force Research Laboratory, Munitions Directorate in June 1999. In Aug 2002, he was assigned to the Flight Training System Program Office of the Aeronautical Systems Center, Wright-Patterson AFB, Ohio where he served as the T-6A ATD Engineer. In Sept 2004, he entered the Graduate School of Engineering and Management, Air Force Institute of Technology. Upon graduation, he will be assigned to the Space and Missile System Center, Detachment 12 at Kirtland AFB, New Mexico.

1. REPORT DATE *(DD-MM-YYYY)* 23-05-2006	**2. REPORT TYPE** **Master's Thesis**		**3. DATES COVERED** *(From – To)* Jun 2005 – Mar 2006
4. TITLE AND SUBTITLE Effect of Hold Times on Fatigue Behavior of Nextel 720™/Alumina Ceramic Matrix Composite at 1200°C in Air and in Steam Environment		**5a. CONTRACT NUMBER**	
		5b. GRANT NUMBER	
		5c. PROGRAM ELEMENT NUMBER	
6. AUTHOR(S) Mehrman, John M., Captain, USAF		**5d. PROJECT NUMBER** 2005-085	
		5e. TASK NUMBER	
		5f. WORK UNIT NUMBER	
7. PERFORMING ORGANIZATION NAMES(S) AND ADDRESS(S) Air Force Institute of Technology Graduate School of Engineering and Management (AFIT/EN) 2950 Hobson Way WPAFB OH 45433-7765		**8. PERFORMING ORGANIZATION REPORT NUMBER** AFIT/GAE/ENY/06-M23	
9. SPONSORING/MONITORING AGENCY NAME(S) AND ADDRESS(ES) AFRL/PRTC Attn: Dr. Ruth Sikorski and Dr Joseph Zelina 1950 5th Street WPAFB OH 45433-7251 DSN: 785-7268		**10. SPONSOR/MONITOR'S ACRONYM(S)**	
		11. SPONSOR/MONITOR'S REPORT NUMBER(S)	
12. DISTRIBUTION/AVAILABILITY STATEMENT APPROVED FOR PUBLIC RELEASE; DISTRIBUTION UNLIMITED.			
13. SUPPLEMENTARY NOTES			

14. ABSTRACT

The aerospace field requires structural materials that can maintain superior mechanical properties while subjected to high temperatures and oxidizing environments. This research investigated the effect of hold times at maximum load on fatigue performance of a Nextel™720/Alumina ceramic matrix composite at 1200°C, explored the influence of environment on material response to cyclic loading with hold times at maximum load, and assessed the effects of loading history on material behavior and environmental durability. The N720/A composite relies on an oxide/oxide composition for inherent oxidation resistance and a porous matrix with no interphase between the fiber and matrix for damage tolerance.

Mechanical testing results showed a significant decrease in material life and performance in a steam environment when compared to tests conducted in a laboratory air environment. Prior fatigue of specimens tested in the air environment resulted in an order of magnitude increase in creep life. Fracture surface observations with a Scanning Electron Microscope showed a correlation between an increase in fiber pull-out and increased time to failure. A qualitative spectral analysis indicated evidence of silicon species migration from the fiber to the matrix, especially in the steam environment. This may be the cause of the decreased creep performance of the material in the steam environment.

15. SUBJECT TERMS
Ceramic Matrix Composites, Composites, Scanning Electron Microscope, Microscopy, Creep, Fatigue, Spectography

16. SECURITY CLASSIFICATION OF:			**17. LIMITATION OF ABSTRACT**	**18. NUMBER OF PAGES**	**19a. NAME OF RESPONSIBLE PERSON** Marina B. Ruggles-Wrenn, AD-23, AFIT/ENY
REPORT U	**ABSTRACT** U	**c. THIS PAGE** U	**UU**	106	**19b. TELEPHONE NUMBER** *(Include area code)* (937) 255-3636, ext 4641; e-mail: Marina.Ruggles-Wrenn@afit.edu